2019

Sparsity Promoting Regularization for Effective Noise Suppression in SPECT Image Reconstruction

Wei Zheng

Si Li

Andrzej Krol

C. Ross Schmidtlein

Xueying Zeng

See next page for additional authors

Original Publication Citation

Zheng, W., Li, S., Krol, A., Schmidtlein, C. R., Zeng, X., & Xu, Y. (2019). Sparsity promoting regularization for effective noise suppression in SPECT image reconstruction. *Inverse Problems*, 35(11), 1-37. doi:10.1088/1361-6420/ab23da

IOP Publishing Inverse Problems

Inverse Problems **35** (2019) 115011 (37pp) https://doi.org/10.1088/1361-6420/ab23da

Sparsity promoting regularization for effective noise suppression in SPECT image reconstruction

Wei Zheng[1], Si Li[2], Andrzej Krol[3], C Ross Schmidtlein[4], Xueying Zeng[5] and Yuesheng Xu[6,7]

[1] School of Mathematics, and Guangdong Provincial Key Lab of Computational Science, Sun Yat-sen University, Guangzhou 510275, People's Republic of China
[2] School of Computer Science and Technology, Guangdong University of Technology, Guangzhou 510006, People's Republic of China
[3] Department of Radiology, Department of Pharmacology, SUNY Upstate Medical University, Syracuse, NY 13210, United States of America
[4] Department of Medical Physics, Memorial Sloan Kettering Cancer Center, New York, NY 10065, United States of America
[5] School of Mathematical Science, Ocean University of China, Qingdao 266100, People's Republic of China
[6] Department of Mathematics and Statistics, Old Dominion University, Norfolk, VA 23529, United States of America

E-mail: y1xu@odu.edu

Received 23 October 2018, revised 26 April 2019
Accepted for publication 22 May 2019
Published 4 October 2019

Abstract

The purpose of this research is to develop an advanced reconstruction method for low-count, hence high-noise, single-photon emission computed tomography (SPECT) image reconstruction. It consists of a novel reconstruction model to suppress noise while conducting reconstruction and an efficient algorithm to solve the model. A novel regularizer is introduced as the nonconvex denoising term based on the approximate sparsity of the image under a geometric tight frame transform domain. The deblurring term is based on the negative log-likelihood of the SPECT data model. To solve the resulting nonconvex optimization problem a preconditioned fixed-point proximity algorithm (PFPA) is introduced. We prove that under appropriate assumptions, PFPA converges to a local solution of the optimization problem at a global $\mathcal{O}(1/k)$ convergence rate. Substantial numerical results for simulation data are presented to demonstrate the superiority of the proposed method in denoising, suppressing artifacts and reconstruction accuracy. We

[7] Author to whom correspondence should be addressed.

simulate noisy 2D SPECT data from two phantoms: hot Gaussian spheres on random lumpy warm background, and the anthropomorphic brain phantom, at high- and low-noise levels (64k and 90k counts, respectively), and reconstruct them using PFPA. We also perform limited comparative studies with selected competing state-of-the-art total variation (TV) and higher-order TV (HOTV) transform-based methods, and widely used post-filtered maximum-likelihood expectation-maximization. We investigate imaging performance of these methods using: contrast-to-noise ratio (CNR), ensemble variance images (EVI), background ensemble noise (BEN), normalized mean-square error (NMSE), and channelized hotelling observer (CHO) detectability. Each of the competing methods is independently optimized for each metric. We establish that the proposed method outperforms the other approaches in all image quality metrics except NMSE where it is matched by HOTV. The superiority of the proposed method is especially evident in the CHO detectability tests results. We also perform qualitative image evaluation for presence and severity of image artifacts where it also performs better in terms of suppressing 'staircase' artifacts, as compared to TV methods. However, edge artifacts on high-contrast regions persist. We conclude that the proposed method may offer a powerful tool for detection tasks in high-noise SPECT imaging.

Keywords: SPECT image reconstruction, denoising, approximate sparsity, nonconvex nonsmooth optimization, staircase artifact

(Some figures may appear in colour only in the online journal)

1. Introduction

Single photon emission computed tomography (SPECT) is a noninvasive molecular imaging modality that requires administration of radioactive tracer to patients. SPECT data are count limited due to the necessity of balancing the collected counts with a patient's radiation dose and imaging time [54]. Using conventional image reconstruction methods, such low-count data leads to very noisy non-clinical quality images. Consequently, suppressing noise while preserving desired image quality in low-count SPECT image reconstruction is an important problem with the potential for significant clinical impact.

A number of researchers have proposed regularization-based reconstruction methods to address the problem of excessive noise in low-count SPECT images [19, 20, 30]. Specifically, Pannin, Zeng, and Gullberg [38] introduced the total variation regularization (TV) model for SPECT image reconstruction. It was initially proposed by Rudin, Osher, and Fatemi [44] for general denoising. TV-type models have also been applied to other image modalities such as CT and MRI due to TV's efficacy in edge-preserving and resolution enhancement [12, 27, 39, 40, 50, 57]. However, TV denoising has certain disadvantages, which might include the loss of fine structures and/or diminished contrast, and the introduction of piecewise constant regions, often referred to as staircase artifacts. All these shortcomings reduce clinical utility of TV-based regularization. In addition, the algorithm developed in [38] for solving the resulting optimization problem converges relatively slowly. The higher-order TV (HOTV) model [30] and the infimal convolution model [55] have been proposed for SPECT reconstruction to suppress the staircase artifacts associated with the TV model. These methods are effective at reducing the artifacts stemming from the first-order TV term with only minimal loss of spatial

resolution. Moreover, the resulting optimization problem for TV regularized SPECT image reconstruction can be efficiently solved using a fixed-point methodology with the proximity operator [33], as was demonstrated by the preconditioned alternating projection algorithm (PAPA) [28, 30].

Total variation methods use the gradient transform (and higher-order gradients) to seek solutions that are sparse in that transform domain. They represent a specific case of a larger methodology known as sparsity-based methods, which are considered to be among the best methods available for image recovery problems such as deblurring, denoising, inpainting, matrix completion, image scale-up, and image compression [22]. The power of these methods stems from the use of particular transforms with which salient image features can be sparsely represented. However, the optimal transform is generally unknown and determination of a best alternative can be difficult. In addition, because the selected transform might not be optimal, the image may still have many small non-sparse elements in the transform domain and may not be truly sparse. Also, the ℓ_0 norm, though considered the best measure of sparseness due to its discrete structure [4, 47], is computationally intractable. An alternative to the ℓ_0 norm, the ℓ_1 norm, though inferior, is typically used instead, as its 'best' convex approximation [21, 34]. Finally, it can be challenging to combine the sparsity-based methods with the denoising task. Despite these difficulties various researchers have introduced a number of transforms providing domains where signals and images may have sparse representations. They include tight frames and dictionaries, which have been widely used in image processing, signal restoration [11, 56, 61], and recently in SPECT image reconstruction [16, 59].

Of various types of sparsifying transforms, wavelet frames have been widely used in image restoration and medical image reconstruction [13, 14, 60]. This approach is based on the discovery that images can be approximately restored (reconstructed) by a few (sparse) wavelet frame coefficients. The tight wavelet frame-based models have been very successful in noise reduction in images due to their flexibility and redundancy property. That motivates us to implement a geometric tight framelet (GTF) system [31] in our novel noise-suppressing regularizer. The GTF system has an additional advantage because it can detect multi-orientation variations of the images.

Under well-defined conditions, the ℓ_1 norm-based model can produce the sparse solution of a particular problem. The resulting model is always convex and can be solved efficiently with many available tools. However, compared with the convex ℓ_1 norm-based model, a nonconvex ℓ_0 norm-based model has certain advantages in the context of image processing [4, 58]. Here, we propose a novel regularization model that combines the sparsity maximization and denoising task, and we introduce the Moreau envelope of the ℓ_0 norm to reformulate the problem. We define the regularization term in the model as the composition of the Moreau envelope of the ℓ_0 norm with the GTF system (L0METF), forming an ℓ_0 norm model based on a tight framelet system. The use of the Moreau envelope has an added advantage in that it separates the sparse representation from the reconstructed denoised image. This allows the reconstructed image to be approximately sparse, preserving small non-sparse components in its transform domain that might otherwise have been lost. Such an approximately sparse model for the SPECT image reconstruction problem integrates the denoising task and sparsity *a priori* information through the use the Moreau envelope of the ℓ_0 norm of a GTF transform.

At present, there are very few efficient algorithms available for the ℓ_0 norm-based models because of both nonconvexity and nondifferentiability of such models. Convex relaxation approach for the ℓ_0 norm model and some greedy pursuit algorithms have been proposed [52, 53]. Iterative hard thresholding algorithms have been extensively studied and applied to solving compressed sensing recovery problems [8]. Zhang, Dong, and Lu proposed the

adapted penalty decomposition method to solve one class of ℓ_0 norm-based minimization models and used the block coordinate descent (BCD) method to solve each of the model's subproblems [60]. More recently, two accelerating algorithms, extrapolation proximal iterative hard thresholding (EPIHT) algorithm and EPIHT with line search (EPIHT-LS), have been proposed to solve the ℓ_0 norm based model [4]. Zeng, Shen, and Xu have also recently developed a two-step fixed-point algorithm to solve an ℓ_0 norm-based model [47]. Attouch, Bolte, Redont, and Soubeyran have proposed the well-known proximal alternating minimization algorithm (PAMA) for solving nonconvex problems [2]. This algorithm has been studied in [9, 20] under the framework of the Kurdyka–Łojasiewicz (KL) property [3]. Under the assumption that the objective function satisfies the KL property, the convergence of sequence generated by PAMA to solve the nonconvex problem is guaranteed to converge to the critical point. In the present study, we develop a preconditioned fixed-point proximity algorithm (PFPA) to solve our proposed model. The algorithm PFPA can be simplified as PAMA. Thus, our method can be incorporated into the PAMA approach based on the framework of the KL property. However, such approach has two deficiencies: (i) methodology of parameter selections is not clear; and (ii) it is only proved that PAMA converges to a critical point of the corresponding nonconvex problem. Based on our observation, we have established that under appropriate conditions PFPA solving the ℓ_0 norm-based model can converge to a local minimizer. We also report the theoretical convergence rate for PFPA. Moreover, EM preconditioner has been applied to accelerate convergence based on its effectiveness, as reported in [28]. We have chosen a variant EM preconditioner in PFPA to accelerate the convergence in practice.

To assess PFPA performance, we compare our method with two state-of-art approaches (TV-PAPA and HOTV-PAPA) and the most common technique (expectation-maximization with Gaussian post-filter, GPF-EM). We note that the GPF-EM model contains solely the fidelity term, while a penalty term (regularizer) is absent. We simulate noisy parallel-beam SPECT data from a phantom with hot Gaussian spheres on warm lumpy background, and an anthropomorphic brain phantom. The following metrics are evaluated: contrast-to-noise ratio (CNR), ensemble variance images (EVI), background ensemble noise (BEN), lesion detectability using channelized hotelling observer (CHO), and reconstruction error via normalized mean square error (NMSE). A task-based strategy is used to determine optimal parameters individually for each metric (e.g. CNR, EVI, BEN, NMSE, and CHO) and each method.

Main contributions of this paper include:

- A novel regularization model exploiting the Moreau envelope of the ℓ_0 norm as a penalty function imposed on the GTF coefficients for the SPECT reconstruction problem is introduced leading to a nonconvex approximately sparse regularization model.
- A preconditioned fixed-point proximity algorithm (FPPA) is developed to solve the resulting nonconvex model, and it is established that the sequence generated by FPPA converges to a local minimizer of the objective function.
- Superior performance of the proposed method in reconstruction of low-count SPECT data, as compared with two state-of-the-art approaches and commonly used technique is validated by numerical experiments.

The remainder of this paper is divided into six sections. In section 2, we propose a nonconvex approximately sparse regularization model using the Moreau envelope of the ℓ_0 norm. In section 3, we characterize the solution of the nonconvex optimization model via a system of fixed-point equations. In section 4, we develop a preconditioned fixed-point proximity algorithm to solve the model based on the characterization. Section 5 is devoted to the convergence result of the iterative algorithm. In section 6, we compare the proposed method

with the existing methods by means of simulations, and we demonstrate numerical results including CNR performance, reconstruction images, BEN, NMSE, and CHO, etc. We arrive at conclusions in section 7.

2. SPECT reconstruction with an approximately sparse regularizer

In this section, we present an approximately sparse denoising reconstruction model for SPECT imaging based upon the emission tomography data model given by

$$g = \text{Poisson}(Af + \gamma), \tag{1}$$

where $g \in \mathbf{R}^m$, $f \in \mathbf{R}^d$, and $\gamma \in \mathbf{R}^m$ are the observed projection data, the unknown tracer distribution, and the additive counts, respectively. The observed data g follows a Poisson distribution [25, 48, 49]. Additive counts may originate from scatter, a hot lab, leakage from other injected patients, and/or numerous other sources. The system matrix $A \in \mathbf{R}^{m\times d}$ describes SPECT imaging process with each entry a_{ij} representing the mean contribution of activity in pixel j to the signal (counts) recorded in the detector bin i, and it can be used to model physical phenomena involved in the imaging process, i.e. attenuation, scatter and detector response, as well as blurring process. In this study we approximate A using a discretization of the Radon transform. The reference [37] adopted the singular value decomposition method and the Sobolev space estimate technique to show that the singular values of Radon transform decay to zero polynomially. Hence, model (1) is ill-posed in the sense that very small changes in the observed data g may lead to disproportionate difference between the true image f and its estimate.

The SPECT reconstruction problem shown in (1) can be formulated as an optimization model via the maximum likelihood (ML) criterion [29, 48, 49]. The ML estimate is obtained by maximizing a log-likelihood function of g conditioned on f. Since the likelihood function in SPECT imaging is assumed to be in a Poisson form, the traditional EM-method [29, 49] attempts to find the expected image by the following model

$$\arg\min_{f\geqslant 0} \left\{ \langle Af, \mathbf{1}\rangle - \langle \ln\left(Af+\gamma\right), g\rangle \right\}, \tag{2}$$

where $\mathbf{1}$ is a column vector of all ones. The objective function in model (2) is closely related to the Kullback–Leibler divergence, which is frequently applied to Poisson data recovery. The Kullback–Leibler divergence of $Af + \gamma$ from g, up to an additive constant, can be defined as [7, 17]

$$D_{\text{KL}}(Af+\gamma, g) := \sum_{i=1}^{m} \left\{ g_i \ln \frac{g_i}{(Af+\gamma)_i} + (Af+\gamma)_i - g_i \right\}.$$

The difference between $D_{\text{KL}}(Af+\gamma, g)$ and the objective function $\langle Af, \mathbf{1}\rangle - \langle \ln(Af+\gamma), g\rangle$ is $\sum_{i=1}^{m}(g_i \ln g_i + \gamma_i - g_i)$, which is independent of the optimization variable f. When one uses an iteration scheme to solve model (2), the fitting noise and the spatial resolution of the reconstructed images increase, as the number of iterations increases, and thus the model produces noisy reconstructed image f [23]. This is typically dealt with by prematurely stopping the iterations followed by some post-smoothing filtration of the reconstructed images. It is based on an ad hoc stopping criterion in an attempt to reach the optimal trade-off between the noise and the spatial resolution. An alternative is to formulate the SPECT reconstruction problem as an optimization model via the penalized maximum likelihood (PML) criterion [24, 25]:

$$\arg\min_{f\geqslant 0}\left\{\langle Af,\mathbf{1}\rangle-\langle\ln(Af+\gamma),g\rangle+\lambda U(f)\right\}, \tag{3}$$

where the regularization term U was introduced to arrive at a more realistic solution, that is, to enforce desirable properties of the estimate. Specifically, model (3) penalizes solutions with low probability, as specified by the prior. Here, λ is a positive regularization parameter and U represents a Gibbs real-valued energy function. Note that the constraint $f\geqslant 0$ is feasible and necessary due to the nonnegativity of the physical tracer distribution.

To address the issue of conventional methods when applied to low-count SPECT data producing noisy images that are not clinically acceptable, we propose a novel reconstruction model that can effectively suppress noise in the low-count (lower-dose or shorter acquisition time) data. To this aim, we design a regularization term that can effectively denoise the underlying image f with only limited and acceptable loss of spatial resolution under a given redundant representation system D during the reconstruction process. Such a redundant system may better capture different image features, and suppress undesirable noise and artifacts. Thus, it provides robust image representations. However, the noise in the latent image will not vanish in the representation space. We call an image *approximately sparse* in an appropriate transform domain, when most of its transform coefficients are very close to zero (instead of actually being zero), in contrast to the remaining few coefficients. For this reason, we approximate the transform coefficients Df by a sparse vector y and minimize the ℓ_2 norm of the discrepancy between the transform coefficients Df and y. Sparsity of a vector is measured by the number of its nonzero components, that is, its ℓ_0 norm. Specifically, we propose the following two-variable optimization model for SPECT reconstruction:

$$\arg\min_{f\geqslant 0}\left\{\langle Af,\mathbf{1}\rangle-\langle\ln(Af+\gamma),g\rangle+\frac{\lambda}{2\beta}\|y-Df\|_2^2+\lambda\|y\|_0:(y,f)\in\mathbf{R}^n\times\mathbf{R}^d\right\}, \tag{4}$$

where β is a positive parameter. Parameter β allows adjusting the approximation of the ℓ_0 norm. In this study, we choose matrix $D\in\mathbf{R}^{n\times d}$ as a discrete tight wavelet frame system, because redundancy is fostering incorporation of prior information to images more efficaciously, as comparing with orthogonal systems. The selected tight wavelet frame system will be described later. Because the objective function of model (4) contains the nonconvex ℓ_0 norm, the optimization model (4) is nonconvex, as well.

Model (4) belongs to a constrained minimization class. For computational convenience we convert it to an unconstrained one by using the indicator function of the nonnegativity constraint set $\mathbf{R}^d_+:=\{x:x\in\mathbf{R}^d \text{ and } x\geqslant 0\}$. Let $\mathbf{H}$ be a finite-dimensional real vector space. The indicator function of a closed convex set $\mathbf{C}$ in $\mathbf{H}$ for a given vector $x\in\mathbf{H}$ is defined by

$$\iota_{\mathbf{C}}(x):=\begin{cases}0 & \text{if } x\in\mathbf{C},\\ +\infty & \text{otherwise.}\end{cases} \tag{5}$$

Employing this notation, we rewrite the constrained minimization model (4) as

$$\arg\min\left\{\langle Af,\mathbf{1}\rangle-\langle\ln(Af+\gamma),g\rangle+\frac{\lambda}{2\beta}\|y-Df\|_2^2+\lambda\|y\|_0+\iota_{\mathbf{R}^d_+}(f):(y,f)\in\mathbf{R}^n\times\mathbf{R}^d\right\}, \tag{6}$$

where $\iota_{\mathbf{R}^d_+}(f)$ is the indicator function defined by (5).

We note that the regularization term appearing in (6) may be describe as the Moreau envelope of the ℓ_0 norm. We recall the definition of the Moreau envelope provided in [35]. For a proper lower semi-continuous function $\phi:\mathbf{H}\to\mathbf{R}\cup\{+\infty\}$, the Moreau envelope of ϕ with positive parameter β is defined as

$$\mathrm{env}_{\beta\phi}(\cdot) := \min\left\{\phi(z) + \frac{1}{2\beta}\|\cdot - z\|_2^2 : \ z \in \mathbf{H}\right\}. \tag{7}$$

Using the Moreau envelope of the ℓ_0 norm, we rewrite minimization model (6) as

$$\arg\min\left\{\langle Af, \mathbf{1}\rangle - \langle \ln(Af+\gamma), g\rangle + \lambda\, \mathrm{env}_{\beta\|\cdot\|_0}(Df) + \iota_{\mathbf{R}^d_+}(f) : f \in \mathbf{R}^d\right\}. \tag{8}$$

We remark that the penalty term $\mathrm{env}_{\beta\|\cdot\|_0}$ is a nonconvex approximation of the ℓ_0 norm $\|\cdot\|_0$, and as $\beta \to 0^+$, $\mathrm{env}_{\beta\|\cdot\|_0} \to \|\cdot\|_0$. In summary, the regularization term $\lambda\ \mathrm{env}_{\beta\|\cdot\|_0}(Df)$ for appropriately chosen parameter β can promote the sparsity of the image f under the redundant system D. Moreover, model (8) is more physically realistic than the ℓ_0-regularized optimization model because images under the redundant system D are approximately sparse, but not absolutely sparse. Finally, introduction of the model (6) facilitates development of efficient optimization algorithms. We note that the ℓ_0-regularized optimization model is an NP hard problem [36]. We explore the computational advantages of model (6) in detail and the equivalence of model (8) and (6) in section 3.

3. Solution of the nonconvex optimization model

In this section, we present the characterization of solutions of model (6) and show the equivalence of models (8) and (6). To characterize the solution of the proposed nonconvex optimization model, we first denote the objective functional in model (6) by

$$G(y,f) := F(f) + \frac{\lambda}{2\beta}\|y - Df\|_2^2 + \lambda\|y\|_0 + \iota_{\mathbf{R}^d_+}(f), (y,f) \in \mathbf{R}^n \times \mathbf{R}^d, \tag{9}$$

where $F(f) := \langle Af, \mathbf{1}\rangle - \langle \ln(Af+\gamma), g\rangle$ is the data fidelity term. We derive that

$$\nabla F(f) = A^t\left(\mathbf{1} - \frac{g}{Af+\gamma}\right), \tag{10}$$

where A^t is the transpose of A. One can check that $\nabla F(f)$ is Lipschitz continuous with constant $L := \frac{\|A\|_2^2\|g\|_\infty}{\gamma^2}$.

We recall both the subdifferential and the proximity operator [5, 35]. The subdifferential of a function ϕ defined on an inner product space $\mathbf{H}$ at a given vector $x \in \mathbf{H}$ is given by the set

$$\partial\phi(x) := \{p : p \in \mathbf{H} \text{ and } \langle z - x, p\rangle + \phi(x) \leqslant \phi(z) \text{ for all } z \in \mathbf{H}\}.$$

An element in $\partial\phi(x)$ is called subgradient. It is closely related to the proximity operator $\mathrm{prox}_{\beta\phi}$ of ϕ defined at $x \in \mathbf{H}$ by

$$\mathrm{prox}_{\beta\phi}(x) := \arg\min_{z\in\mathbf{H}}\left\{\phi(z) + \frac{1}{2\beta}\|z - x\|_2^2\right\}. \tag{11}$$

By recalling equation (7), we note that $\mathrm{prox}_{\beta\phi}$ is the set of the minimizers of function $\mathrm{env}_{\beta\phi}$. The subdifferential and the proximity operator of the function ϕ are closely related: for any $x, p \in \mathbf{H}$,

$$p \in \beta\partial\phi(x) \text{ if and only if } x = \mathrm{prox}_{\beta\phi}(x + p). \tag{12}$$

We then need a useful property of the subdifferential of the indicator function of the set $\mathbf{R}^d_+$. We define

$$\mathbf{P} := \{P : P \text{ is a } d \times d \text{ diagonal matrix with positive diagonal entries}\}$$

and consider the indicator function $\iota_{\mathbf{R}^d_+}$. Note that for any $P \in \mathbf{P}$, the following equation holds

$$P \circ \partial \iota_{\mathbf{R}^d_+} = \partial \iota_{\mathbf{R}^d_+}. \tag{13}$$

With the above preparation, we next present a fixed-point formulation of a solution to the model (6).

Proposition 3.1. *Let λ, β be positive numbers and $D \in \mathbf{R}^{n\times d}$ be a discrete transform matrix. If a pair $(y^\star, f^\star)$ is a solution of model (6), then for any $\alpha \in (0, 1]$ and $P \in \mathbf{P}$,*

$$\begin{cases} y^\star \in \operatorname{prox}_{\alpha\beta\|\cdot\|_0}\left(\alpha D f^\star + (1-\alpha) y^\star\right) \\ f^\star = \operatorname{prox}_{\iota_{\mathbf{R}^d_+}}\left(f^\star + \lambda P D^t\left(y^\star - D f^\star\right) - \beta P \nabla F(f^\star)\right). \end{cases} \tag{14}$$

Proof. Let $(y^\star, f^\star)$ be a solution of model (6). We first show the inclusion relation

$$y^\star \in \operatorname{prox}_{\beta\|\cdot\|_0}\left(D f^\star\right). \tag{15}$$

That is, we shall establish the inequality

$$\|y^*\|_0 + \frac{1}{2\beta}\|y^* - D f^\star\|_2^2 \leqslant \|y\|_0 + \frac{1}{2\beta}\|y - D f^\star\|_2^2, \quad \text{for any } y \in \mathbf{R}^n. \tag{16}$$

According to the assumption of this proposition, we have that

$$G(y^\star, f^\star) \leqslant G(y, f^\star), \quad \text{for any } y \in \operatorname{prox}_{\beta\|\cdot\|_0}(D f^\star). \tag{17}$$

On the other hand, by the definition of the proximity operator, we get from the inclusion $y \in \operatorname{prox}_{\beta\|\cdot\|_0}(D f^\star)$ that

$$\|y\|_0 + \frac{1}{2\beta}\|y - D f^\star\|_2^2 \leqslant \|y^\star\|_0 + \frac{1}{2\beta}\|y^\star - D f^\star\|_2^2.$$

This implies that

$$G(y, f^\star) \leqslant G(y^\star, f^\star), \quad \text{for any } y \in \operatorname{prox}_{\beta\|\cdot\|_0}(D f^\star). \tag{18}$$

Combining (17) and (18), we obtain the equation

$$G(y^\star, f^\star) = G(y, f^\star), \quad \text{for any } y \in \operatorname{prox}_{\beta\|\cdot\|_0}(D f^\star).$$

This yields for any $y \in \operatorname{prox}_{\beta\|\cdot\|_0}(D f^\star)$ that

$$\|y^*\|_0 + \frac{1}{2\beta}\|y^* - D f^\star\|_2^2 = \|y\|_0 + \frac{1}{2\beta}\|y - D f^\star\|_2^2. \tag{19}$$

By employing the proximity operator again, for any $y \in \mathbf{R}^n \setminus \operatorname{prox}_{\beta\|\cdot\|_0}(D f^\star)$, we get that

$$\|y^*\|_0 + \frac{1}{2\beta}\|y^* - D f^\star\|_2^2 < \|y\|_0 + \frac{1}{2\beta}\|y - D f^\star\|_2^2. \tag{20}$$

Combining (19) and (20), we obtain (16). Thus, inclusion relation (15) holds true.

We next show that (15) is equivalent to the first inclusion relation of (14) for any $\alpha \in (0,1]$. Note that (15) is a special case of the first inclusion relation of (14) when $\alpha = 1$. It suffices to prove that (15) implies the first inclusion relation of (14) for any $\alpha \in (0,1)$. By writing the difference $y - Df^\star$ in the right hand side of (16) as the sum of $y - y^\star$ and $y^\star - Df^\star$, expanding the norm of the difference and cancelling the same term in the both sides of the resulting inequality, we get that

$$\|y^\star\|_0 \leqslant \|y\|_0 + \frac{1}{2\beta}\|y - y^\star\|_2^2 + \frac{1}{\beta}\langle y - y^\star, y^\star - Df^\star\rangle, \quad \text{for any } \ y \in \mathbf{R}^n.$$

For any $\alpha \in (0,1)$, we add $\frac{1}{2\alpha\beta}\|\alpha y^\star - \alpha Df^\star\|_2^2$ to both sides of the above inequality and rearrange the right hand side of the resulting inequality to obtain the estimate that for any $y \in \mathbf{R}^n$,

$$\|y^\star\|_0 + \frac{1}{2\alpha\beta}\|y^\star - \left(\alpha Df^\star + (1-\alpha)y^\star\right)\|_2^2 \leqslant \|y\|_0 + \frac{1}{2\alpha\beta}\|y - \left(\alpha Df^\star + (1-\alpha)y^\star\right)\|_2^2 + \frac{\alpha - 1}{2\alpha\beta}\|y - y^\star\|_2^2.$$

Since $\alpha \in (0,1)$, the last term in the right hand side of the inequality above is non-positive. Hence, we have for any $y \in \mathbf{R}^n$ that

$$\|y^\star\|_0 + \frac{1}{2\alpha\beta}\|y^\star - \left(\alpha Df^\star + (1-\alpha)y^\star\right)\|_2^2 \leqslant \|y\|_0 + \frac{1}{2\alpha\beta}\|y - \left(\alpha Df^\star + (1-\alpha)y^\star\right)\|_2^2.$$

That is, we have established the first inclusion relation of (14) for any $\alpha \in (0,1)$.

It remains to prove the second equation of (14). If $(y^\star, f^\star)$ is a solution of model (6), then by virtue of the Fermat rule [41], the inclusion relation holds

$$0 \in \beta\nabla F(f^\star) - \lambda D^t\left(y^\star - Df^\star\right) + \partial\iota_{\mathbf{R}^d_+}\left(f^\star\right),$$

where D^t is the transpose of D. Multiplying the above relation by matrix P from the left and using (12) and (13), we observe that $(y^\star, f^\star)$ satisfies the second equation of (14). □

We remark that proposition 3.1 serves as the basis of the algorithm development to be presented in the next section.

Finally, we establish the equivalence of models (8) and (6).

Proposition 3.2. *Let λ, β be positive numbers, and $D \in \mathbf{R}^{n\times d}$ be a discrete transform matrix. A pair $(y^\star, f^\star)$ is a solution of model (6) if and only if $f^\star$ is a solution of model (8) with $y^\star$ satisfying the first inclusion relation of (14) for any $\alpha \in (0,1]$.*

Proof. We define

$$J(f) := F(f) + \lambda \mathrm{env}_{\beta\|\cdot\|_0}(Df) + \iota_{\mathbf{R}^d_+}(f).$$

By the definitions of the proximity operator and the Moreau envelope, there holds the equation

$$J(f) = G(y,f), \quad \text{for any } \ y \in \mathrm{prox}_{\beta\|\cdot\|_0}(Df). \tag{21}$$

If a pair $(y^\star, f^\star)$ is a solution of model (6), proposition 3.1 implies that $y^\star \in \mathrm{prox}_{\beta\|\cdot\|_0}(Df^\star)$. We confirm that $f^\star$ is the solution of model (8). If this is not true, then there exists a vector $\tilde{f}$

such that $J(\tilde{f}) < J(f^\star)$, which, by (21), implies $G(\tilde{y},\tilde{f}) = J(\tilde{f}) < J(f^\star) = G(y^\star,f^\star)$ for any $\tilde{y} \in \text{prox}_{\beta\|\cdot\|_0}(D\tilde{f})$. This contradicts the assumption that $(y^\star,f^\star)$ is a solution of model (6).

Conversely, if $f^\star$ is a solution of model (8) with $y^\star \in \text{prox}_{\beta\|\cdot\|_0}(Df^\star)$, we assert that $(y^\star,f^\star)$ is a solution of model (6). If this is not true, one can find another vector $\bar{f}$ such that $G(\bar{y},\bar{f}) < G(y^\star,f^\star)$ for any $\bar{y} \in \text{prox}_{\beta\|\cdot\|_0}(D\bar{f})$, which together with (21) implies $J(\bar{f}) < J(f^\star)$. This contradicts the assumption that $f^\star$ is a solution of model (8). □

4. A preconditioned fixed-point proximity algorithm

In this section, we describe the preconditioned fixed-point proximity algorithm that we derived for solving the nonconvex minimization problem (6). Its development relies on certain useful properties of the proximity operator [10, 41], and the iterative computing schemes rely on the fixed-point formulation of model (6) described henceforth.

Below, we present the preconditioned fixed-point proximity algorithm for solving model (6). Based on (14), one can get the following two-step iterative scheme for solving model (6)

$$\begin{cases} y^{k+1} \in \text{prox}_{\alpha\beta\|\cdot\|_0}\Big(\alpha Df^k + (1-\alpha)y^k\Big) \\ f^{k+1} = \text{prox}_{\iota_{\mathbf{R}^d_+}}\Big(f^k + \lambda PD^t\big(y^{k+1} - Df^k\big) - \beta P\nabla F(f^k)\Big), \end{cases} \tag{22}$$

where $\alpha \in (0,1)$. In the first step, we have used a splitting technique with which we have replaced Df by $\alpha Df + (1-\alpha)\, y$. The use of such a technique allows us to guarantee convergence and improve the speed of the iteration convergence by adjusting the parameter α.

The first step of the above iterative scheme is to exploit the sparsity of images in the transform domain, while the second step is to simultaneously tomographically reconstruct and denoise the images. The preconditioned fixed-point proximity algorithm derived from this iterative scheme is denoted by PFPA. Recall that $\text{prox}_{\alpha\beta\|\cdot\|_0}$ is known as the hard thresholding operator. It is easy to see that for every $\alpha, \beta > 0$ and $x \in \mathbf{R}^n$ the proximity operator of the ℓ_0 norm is given by

$$\text{prox}_{\alpha\beta\|\cdot\|_0}(x) = \text{prox}_{\alpha\beta|\cdot|_0}(x_1) \times \text{prox}_{\alpha\beta|\cdot|_0}(x_2) \times \cdots \times \text{prox}_{\alpha\beta|\cdot|_0}(x_n),$$

where

$$\text{prox}_{\alpha\beta|\cdot|_0}(x_i) := \begin{cases} \{x_i\}, & \text{if } |x_i| > \sqrt{2\alpha\beta}, \\ \{x_i, 0\}, & \text{if } |x_i| = \sqrt{2\alpha\beta}, \\ \{0\}, & \text{otherwise.} \end{cases}$$

The proximity operator of the indicator function $\text{prox}_{\iota_{\mathbf{R}^d_+}}$ (the projection operator onto the nonnegative orthant $\mathbf{R}^d_+$) also has an explicit computing expression. That is, for $x \in \mathbf{R}^d$, we have

$$(\text{prox}_{\iota_{\mathbf{R}^d_+}}(x))_i = \max\{x_i, 0\}, i \in \{1, 2, \ldots, d\}.$$

Therefore, algorithm (22) is straightforward for implementation with no need to resorting to more complicated computing methods.

The redundant system D that appears in model (6) and in algorithm (22) has to be specified. Frame theory, developed in [18, 43] that relies on redundant representation of signals using the wavelet frames has been proved very successful in extracting salient features of images

[14, 32, 46]. In this work, we shall choose a geometric tight framelet system [31]. The details are provided hereafter.

The specific geometric tight framelet transform D that we construct here is a block matrix having 18 row blocks D_j, $j = 0, 1, \ldots, 17$. The matrices D_k are represented in terms of the matrices

$$W_0 := \begin{pmatrix} \frac{1}{2} & \frac{1}{4} & & & \frac{1}{4} \\ \frac{1}{4} & \frac{1}{2} & \frac{1}{4} & & \\ & \ddots & \ddots & \ddots & \\ & & \frac{1}{4} & \frac{1}{2} & \frac{1}{4} \\ \frac{1}{4} & & & \frac{1}{4} & \frac{1}{2} \end{pmatrix}, W_1 := \begin{pmatrix} 0 & \frac{\sqrt{2}}{4} & & & -\frac{\sqrt{2}}{4} \\ -\frac{\sqrt{2}}{4} & 0 & \frac{\sqrt{2}}{4} & & \\ & \ddots & \ddots & \ddots & \\ & & -\frac{\sqrt{2}}{4} & 0 & \frac{\sqrt{2}}{4} \\ \frac{\sqrt{2}}{4} & & & -\frac{\sqrt{2}}{4} & 0 \end{pmatrix}, W_2 := \begin{pmatrix} \frac{1}{2} & -\frac{1}{4} & & & -\frac{1}{4} \\ -\frac{1}{4} & \frac{1}{2} & -\frac{1}{4} & & \\ & \ddots & \ddots & \ddots & \\ & & -\frac{1}{4} & \frac{1}{2} & -\frac{1}{4} \\ -\frac{1}{4} & & & -\frac{1}{4} & \frac{1}{2} \end{pmatrix}.$$

Specifically, we define $W_{i,j} := W_i \otimes W_j$ with $i, j = 0, 1, 2$, where $\otimes$ denotes the Kronecker product. We note that $\{W_{i,j}\}_{i,j=0}^{2}$ provides a tight framelet system that is a generalization of the total variation. We then let

$$D_0 := W_{0,0}, \quad D_1 := \frac{\sqrt{2}}{2} W_{0,1}, \quad D_2 := \frac{\sqrt{2}}{2} W_{1,0}, \quad D_3 := \frac{1}{2}(W_{0,1} + W_{1,0}),$$

$$D_4 := \frac{1}{2}(W_{1,0} - W_{0,1}), \quad D_5 := \frac{\sqrt{7}}{3} W_{1,1}, \quad D_6 := \frac{1}{3} W_{0,2}, \quad D_7 := \frac{1}{3} W_{2,0},$$

$$D_8 := \frac{1}{3}(W_{1,1} + W_{0,2} + W_{2,0}), \quad D_9 := \frac{1}{3}(W_{0,2} + W_{2,0} - W_{1,1}),$$

$$D_{10} := \frac{\sqrt{2}}{3}(W_{0,2} - W_{2,0}), \quad D_{11} := W_{2,1}, \quad D_{12} := W_{1,2}, \quad D_{13} := \frac{1}{3} W_{2,2},$$

$$D_{14} := \frac{\sqrt{2}}{3}(W_{0,2} + W_{2,2}), \quad D_{15} := \frac{\sqrt{2}}{3}(W_{0,2} - W_{2,2}),$$

$$D_{16} := \frac{\sqrt{2}}{3}(W_{2,0} + W_{2,2}), \quad D_{17} := \frac{\sqrt{2}}{3}(W_{2,0} - W_{2,2}).$$

Finally, the GTF transform matrix D is given by

$$D := [D_0^t \, D_1^t \, \cdots \, D_{17}^t]^t. \tag{23}$$

One can verify that $D^t D = I$, and as a result, D is a tight framelet transform matrix. It is known that this GTF transform can detect multiorientation and high-order variations of the images. The quotient $\frac{N}{n}$ is generally used to measure the redundancy of a framelet system $\{D_i\}_{i=0}^{N-1}$ for an n-dimensional real inner product space. In comparison with the frame system, $\{W_{i,j}\}_{i,j=0}^{2}$, the framelet system $\{D_i\}_{i=0}^{17}$ has a higher level of redundancy that ensures its resilience to noise in the reconstruction process. Increasing in redundancy of the framelet system leads to a higher level of approximate sparsity in the resulting regularization model. However, it might also increase the computational complexity when solving the corresponding model. Therefore, it requires balancing the level of redundancy in the model and the computational complexity needed to solve the model.

The matrix applied to the latent image f under a proper boundary condition (for example, the periodic boundary condition) is denoted by $D_k f$. We note that $D_k f$ are framelet coefficients of f.

5. Convergence analysis

In this section, we present convergence analysis for the proposed algorithm PFPA. The analysis is done in two stages. We observe that PFPA in fact first searches the invariant support set of a solution of the nonconvex model (6), and then solves a convex minimization problem on the support set. As a result, in stage one of the convergence analysis, we first identify the support set of a solution of the nonconvex model (6) and in stage two, we establish that the solution of the convex model defined on the support set is a local minimizer of the nonconvex model (6). We also show that PFPA solving the proposed nonconvex model has a global $\mathcal{O}(1/k)$ convergence rate.

We now identify the support set of a solution of model (6). To this end, we establish several technical lemmas. The first lemma regards a property of the proximity operator $\mathrm{prox}_{\iota_{\mathbf{R}^d_+}}(\cdot - T\nabla Q(\cdot))$. For a symmetric positive definite (SPD) matrix T, we define the weighted inner product by $\langle x, y\rangle_T := \langle x, T^{-1}y\rangle$ and the corresponding weighted norm by $\|x\|_T := \sqrt{\langle x, x\rangle_T}$. The proximity operator with respect to a SPD matrix T of a convex function ϕ is defined by

$$\mathrm{prox}_{\phi}^{T}(x) := \arg\min_{u}\left\{\phi(u) + \frac{1}{2}\|u - x\|_T^2\right\}.$$

Clearly, $\mathrm{prox}_{\phi}^{I} = \mathrm{prox}_{\phi}$.

Lemma 5.1. *Let T be a positive diagonal matrix and Q be a differentiable convex function defined on $\mathbf{R}^d$. If $v \in \mathbf{R}^d$ is defined by*

$$v := \mathrm{prox}_{\iota_{\mathbf{R}^d_+}}(x - T\nabla Q(x)), \quad \text{for } x \in \mathbf{R}^d,$$

then for all $z \in \mathbf{R}^d_+$ there holds the inequality

$$\|v - z\|_T^2 \leqslant \|x - z\|_T^2 - \|v - x\|_T^2 - 2\langle \nabla Q(x), v - z\rangle. \tag{24}$$

Proof. Direct computation leads to the equation

$$\|v - z\|_T^2 = \|x - z\|_T^2 - \|v - x\|_T^2 + 2\langle T^{-1}(v - x), v - z\rangle. \tag{25}$$

We then split the last term of (25) into the sum of two terms, namely,

$$\langle T^{-1}(v - x), v - z\rangle = \langle T^{-1}(x - T\nabla Q(x) - v), z - v\rangle + \langle -\nabla Q(x), v - z\rangle. \tag{26}$$

The inequality (24) is proved once we establish that the first term in the right hand side of equation (26) is non-positive.

We next prove that $\langle T^{-1}(x - T\nabla Q(x) - v), z - v\rangle \leqslant 0$. One can easily verify that $\mathrm{prox}_{\iota_{\mathbf{R}^d_+}} = \mathrm{prox}_{\iota_{\mathbf{R}^d_+}}^{T}$. Hence, we have that $v = \mathrm{prox}_{\iota_{\mathbf{R}^d_+}}^{T}(x - T\nabla Q(x))$. By the Fermat rule, we get the inclusion

$$x - T\nabla Q(x) - v \in T\partial \iota_{\mathbf{R}^d_+}(v).$$

For details of reasoning for the above inclusion, see, [33]. Multiplying both sides of the above inclusion by T^{-1} and recalling the definition of subdifferential, one arrives at

$$\langle T^{-1}(x - T\nabla Q(x) - v), z - v\rangle \leqslant \iota_{\mathbf{R}^d_+}(z) - \iota_{\mathbf{R}^d_+}(v) = 0$$

for any $z \in \mathbf{R}^d_+$. This estimate combined with equations (25) and (26) completes the proof of (24). □

For given positive numbers λ and β, a vector $y^{k+1} \in \mathbf{R}^n$, an $n \times d$ matrix D, we define a smooth convex function Q at any $f \in \mathbf{R}^d$ by

$$Q(f) := \beta F(f) + \frac{\lambda}{2}\|Df\|_2^2 - \lambda\langle Df, y^{k+1}\rangle. \tag{27}$$

The next lemma is needed in identifying the support set of a solution of model (6).

Lemma 5.2. *Let Q be a function defined by (27). If $\{(y^k, f^k)\}$ is the sequence generated by PFPA, then the inequality*

$$\langle f^{k+1} - f^k, \nabla Q(f^k)\rangle \leqslant -\langle P^{-1}(f^{k+1} - f^k), f^{k+1} - f^k\rangle \tag{28}$$

holds for $P \in \mathbf{P}$.

Proof. By the definition of Q in (27), we derive that

$$\nabla Q(f) = \beta\nabla F(f) + \lambda D^t(Df - y^{k+1}). \tag{29}$$

Since $\{(y^k, f^k)\}$ is the sequence generated by PFPA, combining with (29) we observe that

$$f^{k+1} = \operatorname{prox}_{\iota_{\mathbf{R}^d_+}}\left(f^k - P\nabla Q(f^k)\right).$$

By lemma 5.1, with identifying T, v, x and z in (24) as P, f^{k+1}, f^k, and f^k, respectively, we obtain that

$$\langle f^{k+1} - f^k, \nabla Q(f^k)\rangle \leqslant -\|f^{k+1} - f^k\|_P^2,$$

which completes the proof. □

Let $\omega := \|D\|_2$ and $\widetilde{L} := \beta L + \lambda\omega^2$. The next lemma confirms the Lipschitz continuity of ∇Q.

Lemma 5.3. *If Q is a function defined by (27), then ∇Q is Lipschitz continuous with a Lipschitz constant $\widetilde{L}$, that is, for every $x, v \in \mathbf{R}^d$,*

$$\|\nabla Q(x) - \nabla Q(v)\|_2 \leqslant \widetilde{L}\|x - v\|_2. \tag{30}$$

Proof. By (29), for every $x, v \in \mathbf{R}^d$, we have that

$$\nabla Q(x) - \nabla Q(v) = \beta\nabla F(x) - \beta\nabla F(v) + \lambda D^t D(x - v).$$

Hence, we obtain that

$$\|\nabla Q(x) - \nabla Q(v)\|_2 \leqslant \|\beta(\nabla F(x) - \nabla F(v))\|_2 + \|\lambda D^t D(x - v)\|_2.$$

This inequality together with the Lipschitz continuity of ∇F with a Lipschitz constant L gives (30). □

We are now ready to present a proposition which is at the core of the convergence analysis. To this end, for positive parameters λ, β, and diagonal matrix $P \in \mathbf{P}$, we define a matrix

$$M_{\lambda,\beta,P} := \frac{1}{\beta}(P^{-1} - \frac{\widetilde{L}}{2}I).$$

Proposition 5.4. *Let $\{(y^k,f^k)\}$ be a sequence generated by PFPA with an initial $(y^0,f^0) \in \mathbf{R}^n \times \mathbf{R}^d_+$ for model (6). If $\alpha \in (0,1)$, the positive parameters λ, β, and preconditioner $P \in \mathbf{P}$ are selected such that matrix $M := M_{\lambda,\beta,P}$ is symmetric positive definite, then the following statements hold:*

(i) $G(y^{k+1},f^{k+1}) \leqslant G(y^k,f^k)$ for all $k \geqslant 0$ *and the sequence* $\{G(y^k,f^k)\}$ *converges.*
(ii) $\lim_{k\to\infty} \|y^{k+1} - y^k\|_2 = \lim_{k\to\infty} \|f^{k+1} - f^k\|_2 = 0$.
(iii) The sequence $\{(y^k,f^k)\}$ *has a finite length, that is*

$$\sum_{k=0}^{+\infty} \left(\|y^{k+1} - y^k\|_2^2 + \|f^{k+1} - f^k\|_{M^{-1}}^2\right) < +\infty. \tag{31}$$

(iv) The sequence $\{(y^k,f^k)\}$ *is a Cauchy sequence in* $\mathbf{R}^n \times \mathbf{R}^d_+$.

Proof. We first show (i). This is done by establishing that

$$V := G(y^{k+1},f^{k+1}) - G(y^k,f^k) \leqslant 0, \quad \text{for all } k \geqslant 0.$$

To this end, we write

$$V = V_1 + V_2, \tag{32}$$

where $V_1 := G(y^{k+1},f^{k+1}) - G(y^{k+1},f^k)$ and $V_2 := G(y^{k+1},f^k) - G(y^k,f^k)$. We next estimate V_1 and V_2 separately.

We first consider V_1. By the definition of the objective function (9), noting $f^k, f^{k+1} \in \mathbf{R}^d_+$, we have that

$$V_1 = F(f^{k+1}) + \frac{\lambda}{2\beta}\|y^{k+1} - Df^{k+1}\|_2^2 - F(f^k) - \frac{\lambda}{2\beta}\|y^{k+1} - Df^k\|_2^2.$$

Recalling (27), from a direct computation we obtain that

$$V_1 = \frac{1}{\beta}\left[Q(f^{k+1}) - Q(f^k)\right]. \tag{33}$$

By lemma 5.3, we know that $\nabla Q(f)$ is Lipschitz continuous with constant $\widetilde{L}$. Using lemma 2.1 in [6], we have

$$Q(f^{k+1}) \leqslant Q(f^k) + \langle f^{k+1} - f^k, \nabla Q(f^k)\rangle + \frac{\widetilde{L}}{2}\|f^{k+1} - f^k\|_2^2.$$

Combining this inequality with equation (33) leads to

$$V_1 \leqslant \frac{1}{\beta}\big[\langle f^{k+1}-f^k, \nabla Q(f^k)\rangle + \frac{\widetilde{L}}{2}\|f^{k+1}-f^k\|_2^2\big].$$

By the proof of lemma 5.2, we obtain the estimate that

$$V_1 \leqslant \frac{1}{\beta}\big[-\|f^{k+1}-f^k\|_P^2 + \frac{\widetilde{L}}{2}\|f^{k+1}-f^k\|_2^2\big].$$

Expanding the right hand side of the above inequality and using the definition of matrix $M_{\lambda,\beta,P}$, we find that

$$V_1 \leqslant -\langle M(f^{k+1}-f^k), f^{k+1}-f^k\rangle. \tag{34}$$

Recalling the definition of the weighted norm, estimate (34) becomes

$$V_1 \leqslant -\|f^{k+1}-f^k\|_{M^{-1}}^2. \tag{35}$$

Next, we estimate V_2. Note that

$$V_2 = \lambda\Big(\frac{1}{2\beta}\|y^{k+1}-Df^k\|_2^2 + \|y^{k+1}\|_0 - \frac{1}{2\beta}\|y^k-Df^k\|_2^2 - \|y^k\|_0\Big). \tag{36}$$

Since

$$y^{k+1} \in \operatorname{prox}_{\alpha\beta\|\cdot\|_0}\left(\alpha Df^k + (1-\alpha)\,y^k\right),$$

by the definition of the proximity operator, we have that

$$\|y^{k+1}\|_0 + \frac{1}{2\alpha\beta}\|y^{k+1}-(\alpha Df^k+(1-\alpha)y^k)\|_2^2 \leqslant \|y^k\|_0 + \frac{1}{2\alpha\beta}\|y^k-(\alpha Df^k+(1-\alpha)y^k)\|_2^2.$$

Expanding the quadratic terms in the above inequality and simplifying the resulting inequality yield that

$$\|y^{k+1}\|_0 \leqslant \|y^k\|_0 - \frac{1}{2\alpha\beta}\|y^{k+1}-y^k\|_2^2 - \frac{1}{\beta}\langle y^k-Df^k, y^{k+1}-y^k\rangle. \tag{37}$$

Substituting inequality (37) into the right hand side of (36), we obtain that

$$\begin{aligned} V_2 \leqslant \lambda\Big(&\frac{1}{2\beta}\|y^{k+1}-Df^k\|_2^2 + \|y^k\|_0 - \frac{1}{2\alpha\beta}\|y^{k+1}-y^k\|_2^2 - \frac{1}{\beta}\langle y^k-Df^k, y^{k+1}-y^k\rangle \\ &-\frac{1}{2\beta}\|y^k-Df^k\|_2^2 - \|y^k\|_0\Big). \end{aligned}$$

A direct computation simplifies the right hand side of the above inequality and gives

$$V_2 \leqslant -\frac{\lambda(1-\alpha)}{2\alpha\beta}\|y^{k+1}-y^k\|_2^2. \tag{38}$$

Finally, substituting (35) and (38) into (32) we deduce

$$V \leqslant -\|f^{k+1}-f^k\|^2_{M^{-1}} - \frac{\lambda(1-\alpha)}{2\alpha\beta}\|y^{k+1}-y^k\|_2^2. \tag{39}$$

Because $\frac{\lambda(1-\alpha)}{2\alpha\beta} > 0$ and M is symmetric positive definite, we conclude that $V \leqslant 0$. Moreover, since $\{G(y^k,f^k)\}$ is nonincreasing and bounded from blow, it follows that the sequence $\{G(y^k,f^k)\}$ converges.

(ii) From (39), we have that

$$\frac{\lambda(1-\alpha)}{2\alpha\beta}\|y^{k+1}-y^k\|_2^2 \leqslant -V = G(y^k,f^k) - G(y^{k+1},f^{k+1}) \tag{40}$$

and

$$\|f^{k+1}-f^k\|^2_{M^{-1}} \leqslant -V = G(y^k,f^k) - G(y^{k+1},f^{k+1}). \tag{41}$$

Because $\{G(y^k,f^k)\}$ converges, by letting k tend to infinity in (41) and (40), we obtain that $\lim_{k\to\infty}\|f^{k+1}-f^k\|_{M^{-1}} = 0$ and $\lim_{k\to\infty}\|y^{k+1}-y^k\|_2 = 0$. The norm equivalence of the finite dimensional space in turn implies that $\lim_{k\to\infty}\|f^{k+1}-f^k\|_2 = 0$. This proves item (ii) in this proposition.

(iii) For $K \geqslant 1$, summing the inequality (40) from $k = 0$ to $K-1$ yields

$$\frac{\lambda(1-\alpha)}{2\alpha\beta}\sum_{k=0}^{K-1}\|y^{k+1}-y^k\|_2^2 \leqslant G(y^0,f^0) - G(y^K,f^K).$$

Likewise, summing (41) from $k = 0$ to $K-1$ yields

$$\sum_{k=0}^{K-1}\|f^{k+1}-f^k\|^2_{M^{-1}} \leqslant G(y^0,f^0) - G(y^K,f^K).$$

Let $\rho := \frac{1}{2}\min\{1, \frac{\lambda(1-\alpha)}{2\alpha\beta}\}$. We then have that

$$\sum_{k=0}^{K-1}\left(\|y^{k+1}-y^k\|_2^2 + \|f^{k+1}-f^k\|^2_{M^{-1}}\right) \leqslant \frac{1}{\rho}\left(G(y^0,f^0) - G(y^K,f^K)\right).$$

Since sequence $\{G(y^k,f^k)\}$ converges by statement (i), letting $K \to \infty$, we thus obtain (31).

(iv) By (iii), we have that

$$\sum_{k=K}^{+\infty}\left(\|y^{k+1}-y^k\|_2^2 + \|f^{k+1}-f^k\|^2_{M^{-1}}\right) \to 0, \ \text{ as } \ K \to +\infty.$$

Since M is a SPD matrix, the above relation yields that

$$\sum_{k=K}^{+\infty}\|y^{k+1}-y^k\|_2^2 \to 0, \ \text{ as } \ K \to +\infty \tag{42}$$

and

$$\sum_{k=K}^{+\infty} \|f^{k+1} - f^k\|_{M^{-1}}^2 \to 0, \quad \text{as} \quad K \to +\infty. \tag{43}$$

These observations confirm that sequences $\{y^k\}$ and $\{f^k\}$ are Cauchy sequences. Indeed, for any $m > n > K$, by (42) we have that

$$\|y^m - y^n\|_2 = \left\| \sum_{k=n}^{m-1} (y^{k+1} - y^k) \right\|_2 \leqslant \sum_{k=n}^{m-1} \|y^{k+1} - y^k\|_2 \to 0.$$

From (42), it follows that $\{y^k\}$ is a Cauchy sequence in $\mathbf{R}^n$. Likewise, using (43) we see that $\{f^k\}$ is a Cauchy sequence in $\mathbf{R}^d_+$. We conclude that the sequence $\{(y^k, f^k)\}$ is a Cauchy sequence in $\mathbf{R}^n \times \mathbf{R}^d_+$ and hence a convergent sequence. □

We next confirm the existence of the invariant support set of the sequence generated by PFPA for the nonconvex model (6). For a vector $y \in \mathbf{R}^n$, we denote the index set of all nonzero entries of y by $N(y)$, that is $N(y) = \{i : i \in \mathbf{N}_n, y_i \neq 0\}$, where $\mathbf{N}_n := \{1, 2, \ldots, n\}$. The set $N(y)$ is called the support set of y. The next lemma shows that if the support sets of two consecutive terms of the sequence generated by PFPA are not identical, then the terms must differ by a big margin.

Lemma 5.5. *Let $\{y^k\}$ be the sequence generated by PFPA. If $N(y^k) \neq N(y^{k+1})$, then*

$$\|y^{k+1} - y^k\|_2 \geqslant \sqrt{2\alpha\beta}.$$

Proof. The result may be proved in a way similar to the proof of lemma 3 in [47]. □

Lemma 5.6. *Let $\{(y^k, f^k)\}$ be a sequence generated by PFPA with an initial $(y^0, f^0) \in \mathbf{R}^n \times \mathbf{R}^d_+$ for model (6). If $\alpha \in (0, 1)$, the positive parameters λ, β, and preconditioner $P \in \mathbf{P}$ are selected such that matrix $M := M_{\lambda,\beta,P}$ is symmetric positive definite, then there exists $K > 0$ such that $N(y^k) = N(y^K)$ for all $k \geqslant K$.*

Proof. The proposition 5.4 (ii) ensures that there exists a number $K > 0$ such that

$$\|y^{k+1} - y^k\|_2 < \sqrt{2\alpha\beta}, \quad \text{for all} \quad k \geqslant K. \tag{44}$$

This guarantees that the support set of y^k remains unchanged for all $k \geqslant K$, namely, $N(y^k) = N(y^K)$ when $k \geqslant K$. If this is not true, then there exists $j \geqslant K$ such that $N(y^j) \neq N(y^{j+1})$. However, this combined with lemma 5.5 implies that $\|y^{j+1} - y^j\|_2 \geqslant \sqrt{2\alpha\beta}$. This contradicts (44) and thus completes the proof of the lemma. □

Lemma 5.6 allows us to identify the support set $\Lambda^\star := N(y^k)$ for all $k \geqslant K$, which is a subset of $\mathbf{N}_n$. Associated with the support set $\Lambda^\star$, we introduce a subspace of $\mathbf{R}^n$ by letting

$$S_{\Lambda^\star} := \{y : y \in \mathbf{R}^n, N(y) \subseteq \Lambda^\star\}. \tag{45}$$

Clearly, $S_{\Lambda^\star}$ is convex and moreover, function $G(y, f)$ restricted to $(y, f) \in S_{\Lambda^\star} \times \mathbf{R}^d$ is convex. As a result, for $k \geqslant K$, iteration algorithm PFPA is basically solving a convex optimization model on $S_{\Lambda^\star} \times \mathbf{R}^d$. To make this point clear, for $(y, f) \in \mathbf{R}^n \times \mathbf{R}^d$, we define

$$H(y,f) := F(f) + \frac{\lambda}{2\beta}\|y - Df\|_2^2 + \iota_{S_{\Lambda^\star}}(y) + \iota_{\mathbf{R}^d_+}(f), \tag{46}$$

where $\iota_{S_{\Lambda^\star}}$ is the indicator function of $S_{\Lambda^\star}$. Since $\iota_{S_{\Lambda^\star}}$ is convex, H defined by (46) is convex on $\mathbf{R}^n \times \mathbf{R}^d$. We introduce the convex optimization model

$$\min\{H(y,f) : (y,f) \in \mathbf{R}^n \times \mathbf{R}^d\}. \tag{47}$$

Since function $F(f) + \frac{\lambda}{2\beta}\|y - Df\|_2^2$ is convex and coercive with respect to variables y and f on the unbounded convex set $S_{\Lambda^\star} \times \mathbf{R}^d_+$, the solution set of model (47) is nonempty.

The convex optimization problem (47) is intimately related to the nonconvex optimization problem (6) because the functions H and G are connected by the relation

$$G(y,f) = H(y,f) + \lambda\|y\|_0 - \iota_{S_{\Lambda^\star}}(y). \tag{48}$$

It follows from lemma 5.6 that for $k \geqslant K$, the cardinality $\mathrm{card}(\Lambda^\star) = \|y^k\|_0$ and $\iota_{S_{\Lambda^\star}}(y^k) = 0$. Thus, for sequence $\{(y^k,f^k)\}$ generated by PFPA, we have that

$$G(y^k,f^k) = H(y^k,f^k) + \lambda\mathrm{card}(\Lambda^\star), \quad \text{for all } \ k \geqslant K.$$

Consequently, after step K, the iteration PFPA is essentially solving the convex optimization model (47). We confirm this point in next proposition.

Proposition 5.7. *Let $\{(y^k,f^k)\}$ be a sequence generated by PFPA with an initial $(y^0,f^0) \in \mathbf{R}^n \times \mathbf{R}^d_+$ for model (6). If $\alpha \in (0,1)$, the positive parameters λ, β, and preconditioner $P \in \mathbf{P}$ are selected such that matrix $M_{\lambda,\beta,P}$ is symmetric positive definite, then the subsequence $\{(y^k,f^k)\}_{k\geqslant K}$ converges to a solution of model (47).*

Proof. We first establish that the subsequence $\{(y^k,f^k)\}_{k\geqslant K}$ satisfies the equations

$$\begin{cases} y^{k+1} = \mathrm{prox}_{\iota_{S_{\Lambda^\star}}}\left(\alpha Df^k + (1-\alpha)\, y^k\right) \\ f^{k+1} = \mathrm{prox}_{\iota_{\mathbf{R}^d_+}}\left(f^k + \lambda PD^t\left(y^{k+1} - Df^k\right) - \beta P\nabla F(f^k)\right). \end{cases} \tag{49}$$

For sequence $\{(y^k,f^k)\}$ generated by PFPA, we let

$$d^k := \alpha Df^k + (1-\alpha)\, y^k.$$

Comparing (49) with PFPA (22), we only need to show that the subsequence $\{(y^k,f^k)\}_{k\geqslant K}$ satisfies

$$y^{k+1} = \mathrm{prox}_{\iota_{S_{\Lambda^\star}}}(d^k). \tag{50}$$

Equivalently, we need to prove the inequality

$$\iota_{S_{\Lambda^\star}}(y^{k+1}) + \frac{1}{2}\|y^{k+1} - d^k\|_2^2 \leqslant \iota_{S_{\Lambda^\star}}(y) + \frac{1}{2}\|y - d^k\|_2^2, \quad \text{for all } \ y \in \mathbf{R}^n. \tag{51}$$

To prove (51), we consider two cases: (i) $y \notin S_{\Lambda^\star}$ and (ii) $y \in S_{\Lambda^\star}$. In case (i), since $y \notin S_{\Lambda^\star}$, by the definition of indicator function $\iota_{S_{\Lambda^\star}}$, one obtains that $\iota_{S_{\Lambda^\star}}(y) = \infty$. Thus, inequality (51) holds in this case.

We now consider case (ii). Since by the hypothesis that $\{(y^k,f^k)\}$ is generated by PFPA, we find that

$$y^{k+1} \in \operatorname{prox}_{\alpha\beta\|\cdot\|_0}(d^k).$$

This is equivalent to

$$\|y^{k+1}\|_0 + \frac{1}{2\alpha\beta}\|y^{k+1} - d^k\|_2^2 \leqslant \|y\|_0 + \frac{1}{2\alpha\beta}\|y - d^k\|_2^2, \text{ for all } y \in \mathbf{R}^n. \quad (52)$$

In particular, for any $y \in S_{\Lambda^\star}$, by the definition of $\Lambda^\star$, we have that

$$\|y\|_0 = \operatorname{card}(N(y)) \leqslant \operatorname{card}(\Lambda^\star).$$

We thus get from (52) the inequality

$$\|y^{k+1}\|_0 + \frac{1}{2\alpha\beta}\|y^{k+1} - d^k\|_2^2 \leqslant \operatorname{card}(\Lambda^\star) + \frac{1}{2\alpha\beta}\|y - d^k\|_2^2, \text{ for } y \in S_{\Lambda^\star}. \quad (53)$$

By lemma 5.6, we have that $N(y^{k+1}) = \Lambda^\star$ for $k \geqslant K$. Thus, inequality (53) becomes

$$\frac{1}{2\alpha\beta}\|y^{k+1} - d^k\|_2^2 \leqslant \frac{1}{2\alpha\beta}\|y - d^k\|_2^2, \text{ for } y \in S_{\Lambda^\star}. \quad (54)$$

By the definition of $S_{\Lambda^\star}$ it is clear that $y^{k+1} \in S_{\Lambda^\star}$. It follows that $\iota_{S_{\Lambda^\star}}(y^{k+1}) = \iota_{S_{\Lambda^\star}}(y) = 0$ for $y \in S_{\Lambda^\star}$. This together with (54) gives us that

$$\iota_{S_{\Lambda^\star}}(y^{k+1}) + \frac{1}{2}\|y^{k+1} - d^k\|_2^2 \leqslant \iota_{S_{\Lambda^\star}}(y) + \frac{1}{2}\|y - d^k\|_2^2 \text{ for } y \in S_{\Lambda^\star}.$$

Summarizing the results proved above we conclude inequality (51) and thus inclusion relation (50).

We next establish the result that $\{(y^k, f^k)\}_{k\geqslant K}$ converges to a solution of model (47). By lemma 5.6, we observe that $\{(y^k, f^k)\}_{k\geqslant K} \subset S_{\Lambda^\star} \times \mathbf{R}^d_+$. This together with Item (iv) of proposition 5.4 ensures that the subsequence $\{(y^k, f^k)\}_{k\geqslant K}$ is a convergent sequence in $S_{\Lambda^\star} \times \mathbf{R}^d_+$. Let $(y^\star, f^\star)$ denote its limit point. Since $S_{\Lambda^\star} \times \mathbf{R}^d_+$ is complete, we have that $(y^\star, f^\star) \in S_{\Lambda^\star} \times \mathbf{R}^d_+$. Since subsequence $\{(y^k, f^k)\}_{k\geqslant K}$ satisfies (49), we conclude that $(y^\star, f^\star)$ satisfies the fixed-point equations

$$\begin{cases} y^\star = \operatorname{prox}_{\iota_{S_{\Lambda^\star}}}\left(\alpha D f^\star + (1-\alpha)\, y^\star\right), \\ f^\star = \operatorname{prox}_{\iota_{\mathbf{R}^d_+}}\left(f^\star + \lambda P D^t\left(y^\star - D f^\star\right) - \beta P \nabla F(f^\star)\right). \end{cases} \quad (55)$$

By employing (12), we observe that the fixed-point equations (55) are equivalent to the inclusion relations

$$0 \in \frac{\lambda}{\beta}(y^\star - Df^\star) + \partial\iota_{S_{\Lambda^\star}}(y^\star) \text{ and } 0 \in \nabla F(f^\star) - \frac{\lambda}{\beta}D^t(y^\star - Df^\star) + \partial\iota_{\mathbf{R}^d_+}(f^\star), \quad (56)$$

where ∂ denotes the Fréchet subdifferntial. Applying $\partial\iota_{S_{\Lambda^\star}} = \frac{\lambda}{\alpha\beta}\partial\iota_{S_{\Lambda^\star}}$ and (13) to the first and second inclusions above, respectively, inclusion relations (56) are equivalent to

$$\alpha(Df^\star - y^\star) \in \partial\iota_{S_{\Lambda^\star}}(y^\star) \text{ and } \lambda P D^t\left(y^\star - Df^\star\right) - \beta P \nabla F(f^\star) \in \partial\iota_{\mathbf{R}^d_+}(f^\star).$$

Namely,

$$0 \in \partial_y H(y^\star, f^\star) \ \text{ and } \ 0 \in \partial_f H(y^\star, f^\star).$$

According to the Fermat rule, we conclude that $(y^\star, f^\star)$ is a solution of model (47). □

The next lemma confirms that a solution of convex model (47) is a local minimizer of the nonconvex model (6).

Lemma 5.8. *If $(y^\star, f^\star)$ is a solution of the convex model (47), then $(y^\star, f^\star)$ is a local minimizer of $G(y,f)$ in the nonconvex model (6).*

Proof. We prove that there exists $\delta > 0$ such that

$$G(y^\star, f^\star) \leqslant G(y^\star + \nabla y, f^\star + \nabla f), \ \text{ for all } \ \|\nabla y\| \leqslant \delta, \|\nabla f\| \leqslant \delta. \tag{57}$$

We first consider the case $f^\star + \nabla f \notin \mathbf{R}^d_+$. According to the definition of the indicator function, we see that $\iota_{\mathbf{R}^d_+}(f^\star + \nabla f) = +\infty$. We then get immediately that in this case $G(y^\star, f^\star) \leqslant G(y^\star + \nabla y, f^\star + \nabla f)$.

It remains to consider the case $f^\star + \nabla f \in \mathbf{R}^d_+$. To this end, we let

$$h(y,f) := F(f) + \frac{\lambda}{2\beta}\|y - Df\|_2^2 \ \text{ for } \ (y,f) \in \mathbf{R}^n \times \mathbf{R}^d.$$

Thus,

$$H(y,f) = h(y,f) + \iota_{S_{\Lambda^\star}}(y) + \iota_{\mathbf{R}^d_+}(f).$$

By hypothesis, for any ∇y and ∇f, we have that

$$H(y^\star, f^\star) \leqslant H(y^\star + \nabla y, f^\star + \nabla f). \tag{58}$$

We consider two subcases: (i) $N(\nabla y) \subset \Lambda^\star$ and (ii) $N(\nabla y) \not\subset \Lambda^\star$. Choose $\sigma_1 := \min_{i \in \Lambda^\star}\{|y_i^\star|\}$.

We first consider subcase (i). From (58), we have that

$$h(y^\star, f^\star) + \iota_{S_{\Lambda^\star}}(y^\star) + \iota_{\mathbf{R}^d_+}(f^\star) \leqslant h(y^\star + \nabla y, ^\star + \nabla f) + \iota_{S_{\Lambda^\star}}(y^\star + \nabla y) + \iota_{\mathbf{R}^d_+}(f^\star + \nabla f).$$

Since $N(\nabla y) \subset \Lambda^\star$, this implies $y^\star + \nabla y \in S_{\Lambda^\star}$. Thus, the above inequality yields

$$h(y^\star, f^\star) \leqslant h(y^\star + \nabla y, ^\star + \nabla f). \tag{59}$$

When $\|\nabla y\|_\infty < \sigma_1$, we have

$$\operatorname{card}\big(N(y^\star + \nabla y)\big) = \operatorname{card}(\Lambda^\star).$$

This together with (59) give us that

$$G(y^\star, f^\star) \leqslant G(y^\star + \nabla y, f^\star + \nabla f).$$

We next consider subcase (ii). The continuity of function h implies that

$$\lim_{\nabla y, \nabla f \to 0} h(y^\star + \nabla y, f^\star + \nabla f) = h(y^\star, f^\star).$$

Hence, there exist $\sigma_2 > 0$ and $\sigma_3 > 0$ such that

$$h(y^\star, f^\star) \leqslant h(y^\star + \nabla y, f^\star + \nabla f) + \lambda, \tag{60}$$

whenever $\|\nabla y\|_\infty < \sigma_2$ and $\|\nabla f\|_\infty < \sigma_3$. Let $\sigma := \min\{\sigma_1, \sigma_2\}$. When $\|\nabla y\|_\infty < \sigma$, we have that

$$\operatorname{card}\big(N(y^\star + \nabla y)\big) \geqslant \operatorname{card}(\Lambda^\star) + 1. \tag{61}$$

By a direct computation, we obtain that

$$G(y^\star, f^\star) - G(y^\star + \nabla y, f^\star + \nabla f) = h(y^\star, f^\star) + \lambda \operatorname{card}(\Lambda^\star) - h(y^\star + \nabla y, f^\star + \nabla f) - \lambda \operatorname{card}\big(N(y^\star + \nabla y)\big).$$

This together with (60) and (61) leads to

$$G(y^\star, f^\star) - G(y^\star + \nabla y, f^\star + \nabla f) \leqslant 0.$$

Choosing $\delta := \min\{\sigma, \sigma_3\}$, we conclude that (57) holds true. □

We are now ready to present the main result of this section.

Theorem 5.9. *Let $\{(y^k, f^k)\}$ be a sequence generated by PFPA with an initial $(y^0, f^0) \in \mathbf{R}^n \times \mathbf{R}^d_+$ for model (6). If $\alpha \in (0, 1)$, the positive parameters λ, β, and preconditioner $P \in \mathbf{P}$ are selected such that matrix $M_{\lambda,\beta,P}$ is symmetric positive definite, then $\{(y^k, f^k)\}$ converges to a local minimizer of model (6).*

Proof. By proposition 5.7, the sequence $\{(y^k, f^k)\}$ converges to a solution $(y^\star, f^\star)$ of model (47). It follows from lemma 5.8 that $(y^\star, f^\star)$ is a local minimizer of model (6). □

The following corollary specializes theorem 5.9 to the case of D being a tight frame transform, that is, $D^t D = I$.

Corollary 5.10. *Let $D \in \mathbf{R}^{n\times d}$ be a tight frame system. If positive parameters λ, β and matrix $P \in \mathbf{P}$ are selected such that the inequality $\beta L + \lambda < 2\|P\|_\infty$ holds, then the sequence $\{(y^k, f^k)\}$ generated by PFPA converges to a local minimizer of model (6).*

Proof. For $P \in \mathbf{P}$, if positive parameters λ, β and matrix P are selected such that $\beta L + \lambda < 2\|P\|_\infty$, then one can verify $M_{\lambda,\beta,P}$ is symmetric positive definite for $\omega = 1$. By theorem 5.9, the sequence $\{(y^k, f^k)\}$ generated by PFPA converges to a local minimizer of model (6). □

The following result shows the convergence rate for PFPA.

Theorem 5.11. *Let $\{(y^k, f^k)\}$ be a sequence generated by PFPA with an initial $(y^0, f^0) \in \mathbf{R}^n \times \mathbf{R}^d_+$ for model (6). If $\alpha \in (0, 1)$, the positive parameters λ, β, and preconditioner $P \in \mathbf{P}$ are selected such that matrix $M_{\lambda,\beta,P}$ is symmetric positive definite, then there exists a real number $\rho > 0$ such that for any integer $K' > 0$*

$$\inf_{k \geqslant K'} \left\{ \|y^{k+1} - y^k\|_2^2 + \|f^{k+1} - f^k\|^2_{M^{-1}_{\lambda,\beta,P}} \right\} \leqslant \frac{1}{\rho K'} \left(G(y^0, f^0) - G(y^\star, f^\star) \right).$$

Proof. By the proof of Item (iii) of proposition 5.4, for any integer $K' > 0$, we have that

$$\sum_{k=0}^{K'-1}\left(\|y^{k+1}-y^{k}\|_2^2+\|f^{k+1}-f^{k}\|^2_{M^{-1}_{\lambda,\beta,P}}\right)\leqslant\frac{1}{\rho}\left(G(y^0,f^0)-G(y^{K'},f^{K'})\right),$$

where

$$\rho:=\frac{1}{2}\min\left\{1,\frac{\lambda(1-\alpha)}{2\alpha\beta}\right\}.$$

By Item (i) of proposition 5.4, we obtain that

$$G(y^\star,f^\star)\leqslant G(y^{K'},f^{K'}).$$

Consequently, we conclude that

$$\inf_{k\geqslant K'}\{\|y^{k+1}-y^{k}\|_2^2+\|f^{k+1}-f^{k}\|^2_{M^{-1}_{\lambda,\beta,P}}\}\leqslant\frac{1}{\rho K'}\left(G(y^0,f^0)-G(y^\star,f^\star)\right)$$

proving the result of this theorem. □

This theorem confirms that theoretically the proposed algorithm can reach a $\mathcal{O}(1/k)$ convergence rate.

6. Numerical experiments

We apply the proposed algorithm PFPA to solve the L0METF-regularized optimization model (8), leading to a novel reconstruction method L0METF-PFPA. We compare the method L0METF-PFPA with: (1) conventional EM algorithm with Gaussian post-filter (GPF-EM) [29, 49], (2) PAPA with a TV regularizer (TV-PAPA) [28], and (3) PAPA with a HOTV regularizer (HOTV-PAPA) [30].

A number of phantoms are used to simulate noisy SPECT data, see below. The data are reconstructed using the aforementioned four methods. In emission computed tomography (SPECT and PET) inverse problem models are nonlinear due to the random nature of photon emission and detection. Because the geometric sensitivity, scatter (and randoms in PET), and photon attenuation, are non-stationary, the reconstructed images are shift-variant with non-stationary noise properties.

For this reason, one needs to carefully select metrics suitable for studying quality of images produced by such systems. In the present study, to evaluate image quality, we apply contrast-to-noise ratio (CNR), ensemble variance images (EVI), background ensemble noise (BEN), channelized hotelling observer (CHO) and normalized mean-squared error (NMSE). For evaluating the accuracy of the reconstruction of the data, we analyze line profiles through reconstructed images, and compare them with ground truth—the line profiles through the phantoms. We establish that the method L0METF-PFPA created images with better considered image quality metrics, as compared with GPF-EM, TV-PAPA, and HOTV-PAPA.

6.1. Numerical phantom and simulations

The spatially inhomogeneous (lumpy) backgrounds are commonly observed in molecular imaging (PET and SPECT). They result from several causes including nonuniform distribution of radioactive metabolites in blood, highly variable blood perfusion, irregular tumor vasculature, and heterogeneous tracer kinetics in blood, normal tissue and tumor. Under such circumstances, the model observer detection performance becomes nonlinear and thus more difficult to assess, as compared to the uniform background [42]. For this reason, in an attempt to perform more realistic model observer studies, we used a phantom with the spatially inhomogeneous warm background [30]. The lumpy warm background was obtained by superimposing randomly distributed Gaussian blobs within a cylinder with fixed uniform activity (diameter 20.8 cm and height 14.1 cm). The lumpy background has the advantage of being statistically tractable and stationary. It can be used to simulate variability of emission tomographic images and it has also been proven useful in the investigation of image reconstruction algorithms [1]. Six 'hot' Gaussian spheres representing lesions are inserted to the lumpy background (see figures 1(a) and (b)). The spheres, together with the lumpy background, form the phantom f which is the object to be reconstructed. We define the mean background as an average of activity in the cylinder without hot spheres. The ratio of maximum activity of the hot spheres to mean background is set to 8:1. The radii of the six spheres are $9, 8, 7, 6, 5$, and 4 mm, respectively. The phantom is defined in 128×128 matrix.

In addition, an emission tomography brain image in a 256×256 matrix is used as a numerical phantom for simulating SPECT data from human brain (figure 1(c)). In this case, the mean background activity is 0.4. In all the reconstructions, the additive counts term $\gamma = 0.001$ is used, which avoids division by zero in the reconstruction algorithms.

To simulate the system matrix in a simplified manner, neither scatter nor attenuation is modeled, and ideal detectors (no blurring, no deadtime losses, no septal penetration, etc) are assumed. A parallel-collimated SPECT projection data consists of 120 views in a 128-dimensional detector array with a 2.2 mm detector bin size. We assume that the system matrix A is defined by a geometric projection matrix only, i.e. $a_{ij} = \sum_{k=1}^{4} l_{ij}^{k}$, where l_{ij}^{k} is the length of intersection with pixel j of the kth ray normal to the detector face and directed towards the detector bin i (see figure 2(a)). For better trade-off between accuracy and computational efficiency, we use four rays in the calculation of a_{ij} for each detector bin. Assuming that the system matrix A has 128×120 rows and 128×128 columns, we extract a submatrix from the system matrix A (see figure 2(b)). This submatrix is sparse, and we observe that A is also sparse. Based on the noise-free projection Af, we use the built-in Matlab *imnoise* function to create Poisson-distributed SPECT projection data with two different total photon count numbers per view: 90 K and 64 K. The phantom with lower (more noisy) and higher (less noisy) total counts are called 'high-noise phantom' and 'low-noise phantom', respectively. Simulated SPECT projection sinograms examples for the Gaussian sphere phantom for the two noise levels are shown in figure 3. We apply the same procedure to the anthropomorphic brain phantom, and obtain the SPECT projection data (sinogram) with 390 K photon counts and size of 256×120.

6.2. Review of three competing reconstruction methods

In this subsection, we review three competing reconstruction methods that will be compared to the proposed method (L0METF-PFPA).

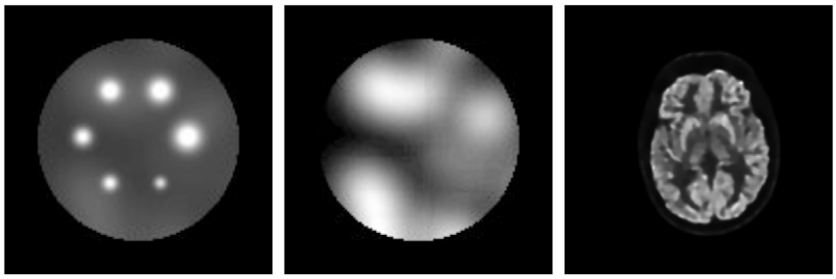

Figure 1. Transaxial cross-sections through phantom containing: (a) and (b) Background with and without six Gaussian spheres (radii = 4, 5, 6, 7, 8, and 9 mm), respectively with maximum-activity-to-mean-background ratio of 8:1, size 128 × 128; (c) An anthropomorphic brain phantom with size 256 × 256.

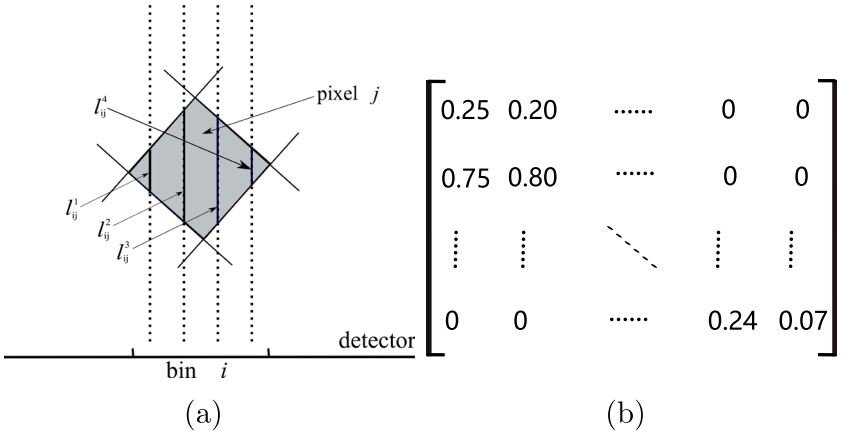

Figure 2. An example of the geometric SPECT system matrix used for the Gaussian spheres phantom reconstruction: (a) each system matrix entry a_{ij} is estimated by using the lengths of intersections l_{ij}^k with pixel j of four rays normal to the detector face and directed towards the detector bin i; (b) the submatrix $A(6:14, 1153:1278)$ of the system matrix A.

- **GPF-EM**: While OSEM [26], an ordered-subset version of ML-EM [49], is the most widely used method for SPECT and PET image reconstruction, in this study we used ML-EM to simplify algorithm development. The ML-EM method attempts to find the most likely image given the data, i.e., the image that maximizes the likelihood of producing the acquired projection data. For Poisson data, the EM algorithm is applied to solve the model described in (2). It is well known that for unconstrained ML-EM, as iterations increase the fitting noise of reconstructed images also increases. In the case of reconstructing sparse objects, the reconstructed images can be strongly affected by a specific effect of the noise called checkerboard effect [7, 37]. A common solution to regularization of the reconstructed images is starting from a uniform initial image, thenceforth stopping the algorithm at a predetermined iteration number, and subsequently removing excessive noise by application of a smoothing post-filter. We note that stopping iterations too early can lead to poor detail recovery, especially in low count regions. In the experi-

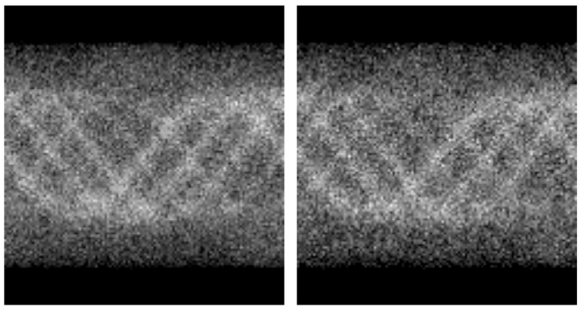

(a) (b)

Figure 3. Simulated SPECT projection data for the Gaussian spheres phantom: (a) 90 K; (b)64 K counts.

ments, we stop ML-EM at the 100th iteration and apply a 2D Gaussian post-smoothing filter to obtain the GPF-EM images.

- **TV-PAPA**: In this method, images are reconstructed using PAPA algorithm with a penalty term in the form of composition of a convex nonnegative function φ_1 and a first order difference matrix B_1. The model of TV-PAPA method is based on (3) with the regularization term,

$$\lambda U(f) := \lambda\varphi_1(B_1 f). \tag{62}$$

PAPA is developed to solve the regularization model, where given any initial (f^0, b^0), for any $k = 0, 1, \ldots$, the TV-PAPA iterative scheme reads

$$\begin{cases} h^k = \text{prox}_{\iota_{\mathbf{R}^d_+}}\left(PA^t\frac{g}{Af^k+\gamma} - \lambda\mu PB_1^t b^k\right), \\ b^{k+1} = \left(I - \text{prox}_{(\lambda/\mu)\varphi_1}\right)\left(b^k + B_1 h^k\right), \\ f^{k+1} = \text{prox}_{\iota_{\mathbf{R}^d_+}}\left(PA^t\frac{g}{Af^k+\gamma} - \lambda\mu PB_1^t b^{k+1}\right). \end{cases}$$

In the above scheme, $b \in \mathbf{R}^{2d}$ is the dual variable in the gradient domain, P is the $d \times d$ diagonal, positive definite, preconditioning matrix, and μ is a positive parameter. Following [28], we choose P as the diagonal matrix $P^k = \text{diag}\left(f^k/A^t\mathbf{1}\right)$ at the kth iteration, and $\mu = 1/(2\lambda\|B_1\|_2^2\|P^k\|_\infty)$. TV-PAPA has several advantages over other algorithms designed to solve the model with the regularization term (62). It outperforms the nested EM-TV method [45] in the convergence speed while providing comparable image quality. It also surpasses GPF-EM in all aspects including the convergence speed, the noise suppression and the lesion detectability. However, TV-PAPA has some disadvantages. It may suffer from loss of fine structure or contrast and may produce staircase artifacts.

- **HOTV-PAPA**: In this case, images are reconstructed using a penalty term in the form of composition of convex nonnegative functions φ_1 and φ_2, and the first and the second order difference matrices B_1 and B_2. The regularization term of HOTV-PAPA model reads

$$\lambda U(f) := \lambda_1\varphi_1\left(B_1 f\right) + \lambda_2\varphi_2(B_2 f).$$

PAPA is utilized to solve the regularization model, therefore we denote this method by HOTV-PAPA. The HOTV-PAPA [30] is able to significantly reduce staircase artifacts

while avoiding unacceptable resolution loss at tolerable noise level. When dealing with high-noise projection data, we find that the staircase artifacts in the reconstructed images are not adequately suppressed, which likely results in lowering the contrast-to-noise ratio (CNR) and the detectability for the lesions.

We have two remarks about P and D that appear in the proposed algorithm PFPA.

Remark 6.1. The PFPA, convergence of which we proved in section 5, uses a fixed matrix P. Motivated by the PAPA algorithm, we change the preconditioner P dynamically from step to step, and we choose P in PFPA as the diagonal matrix $P^k = \tau_k \mathrm{diag}\left(f^k/A^t\mathbf{1}\right)$ at the kth iteration. We adopt an adaptive strategy for updating parameter τ. The algorithmic parameter τ_k is decreasing such that algorithm 1 is convergent by theorem 5.9. Consequently, the selection of matrix P^k depends on the current reconstruction f^k and the algorithmic parameter τ_k. Therefore, to solve model (6), we propose a dynamic PFPA shown as algorithm 1.

Algorithm 1. Preconditioned fixed-point proximity (PFPA) algorithm for SPECT reconstruction.

Preparation: ∇F and D are defined in (10) and (23), respectively. The parameter $\alpha \in (0,1)$, λ, β and τ are positive integers.
Initialization: $y^k \leftarrow y^0$, $f^k \leftarrow f^0$, $\tau_k \leftarrow \tau$ and $\tau_{\min} = \frac{\tau}{2} \times 10^{-10}$.
repeat
Step 1: If $k > 1$, $\tau_k > \tau_{\min}$ and $\|f^k - f^{k-1}\|_2/\|f^{k-1}\|_2 > \|f^{k-1} - f^{k-2}\|_2/\|f^{k-2}\|_2$, update $\tau_k \leftarrow \max\{\tau_k/2, \tau_{\min}\}$
Step 2: $P^k \leftarrow \tau_k \mathrm{diag}\left(f^k/A^t\mathbf{1}\right)$
Step 3: $y^{k+1} \leftarrow \mathrm{prox}_{\alpha\beta\|\cdot\|_0}\left(\alpha D f^k + (1-\alpha)\, y^k\right)$
Step 4: $f^{(k+1)} \leftarrow \mathrm{prox}_{\iota_{\mathbf{R}^d_+}}\left(f^k + \lambda P^k D^t\left(y^{k+1} - D f^k\right) - \beta P^k \nabla F(f^k)\right)$
until 'Convergence'

Remark 6.2. In practical implementation of algorithms, f is a two dimensional signal. We notice that using formulating matrices for tight frame transforms and difference operators provides a convenient way to present algorithms and analysis. Nonetheless, the actual construction of matrix representations for $D_k, k = 0, 1, 2, \ldots, 17$ and $B_i, i = 1,2$ is not necessary, because it can be accomplished by the associated operators applied to the latent two dimensional image f [30, 47].

More details on the GTF matrix D are provided hereafter. Exploiting the tensor product of the averaging mask, the first-order difference mask, and the second-order difference mask, we can obtain the corresponding filters $\{L_i\}_{i=0}^{17}$ associated with the tight framelet transform matrix D. Specifically, the masks are sequences of Fourier coefficients of the corresponding filters, which are given as follows

$$\omega_0 = \frac{1}{4}[1\ 2\ 1],\ \ \omega_1 = \frac{\sqrt{2}}{4}[1\ 0\ -1],\ \ \omega_2 = \frac{1}{4}[-1\ 2\ -1]. \tag{63}$$

The 2D refinement masks denoted by $M_{i,j}$ can be calculated by

$$M_{i,j} := \omega_i^t \omega_j,\ \ i,j = 0,1,2,$$

where ω_i and ω_j are defined by (63). Let

Table 1. Optimal parameters (λ, β, τ) for four metrics at two different noise levels for L0METF-PFPA method.

Method	Low-noise phantom (90 K counts)	High-noise phantom (64 counts)
CNR	$(1.9 \times 10^{-2}, 4 \times 10^{-6}, 1.7 \times 10^{5})$	$(1.3 \times 10^{-2}, 2 \times 10^{-6}, 3.5 \times 10^{5})$
BEN	$(1.8 \times 10^{-2}, 4 \times 10^{-6}, 1.72 \times 10^{5})$	$(1.8 \times 10^{-2}, 1 \times 10^{-6}, 7 \times 10^{5})$
NMSE	$(1.8 \times 10^{-2}, 4 \times 10^{-6}, 1.72 \times 10^{5})$	$(1.8 \times 10^{-2}, 1 \times 10^{-6}, 7 \times 10^{5})$
CHO	$(2.1 \times 10^{-2}, 9 \times 10^{-6}, 4.6 \times 10^{4})$	$(1.4 \times 10^{-2}, 4 \times 10^{-6}, 1.8 \times 10^{5})$

$$L_0 := M_{0,0},\ L_1 := \frac{\sqrt{2}}{2}M_{0,1},\ L_2 := \frac{\sqrt{2}}{2}M_{1,0},\ L_3 := \frac{1}{2}(M_{0,1} + M_{1,0}),$$

$$L_4 := \frac{1}{2}(M_{1,0} - M_{0,1}),\ L_5 := \frac{\sqrt{7}}{3}M_{1,1},\ L_6 := \frac{1}{3}M_{0,2},\ L_7 := \frac{1}{3}M_{2,0},$$

$$L_8 := \frac{1}{3}(M_{1,1} + M_{0,2} + M_{2,0}),\ L_9 := \frac{1}{3}(M_{0,2} + M_{2,0} - M_{1,1}),$$

$$L_{10} := \frac{\sqrt{2}}{3}(M_{0,2} - M_{2,0}),\ L_{11} := M_{2,1},\ L_{12} := M_{1,2},\ L_{13} := \frac{1}{3}M_{2,2},$$

$$L_{14} := \frac{\sqrt{2}}{3}(M_{0,2} + M_{2,2}),\ L_{15} := \frac{\sqrt{2}}{3}(M_{0,2} - M_{2,2}),$$

$$L_{16} := \frac{\sqrt{2}}{3}(M_{2,0} + M_{2,2}),\ L_{17} := \frac{\sqrt{2}}{3}(M_{2,0} - M_{2,2}).$$

We thus obtain the filters which we utilize in the implementation of the algorithm PFPA. We remark that $\{L_i\}_{i=0}^{17}$ are consistent with $\{D_i\}_{i=0}^{17}$. They are just different formulations for the GTF. We verify that all matrices $L_k, k = 0, 1, \ldots, 17$ are size of 3×3 with L_0 acts as low-pass filters and $L_k, k = 1, 2, \ldots, 17$, act as high-pass filters for the corresponding framelet system. Specifically, L_0 acts as a weighted averaging operator, and L_1, L_2, L_3, L_4 act as the Sobel operators (scaled by a constant) in the horizontal, vertical, $-\pi/4$, and $\pi/4$ directions, respectively. L_8 acts as the second order difference operator in the $\pi/4$ direction while L_9 acts as the second order difference operator in the $-\pi/4$ direction; L_{14} and L_{15} serve as the second order difference operator in the horizontal direction while L_{16} and L_{17} serve as the second order difference operator in the vertical direction. The other not yet discussed operators can be viewed as composite of the averaging, Sobel, and the difference operators, or they can act separately. As an example consider L_{10}. We realize that because $L_{10} = L_{14} + L_{15} - \frac{\sqrt{2}}{2}(L_8 + L_9)$, L_{10} acts as composite of the second order difference operators in the horizontal, $\pi/4$, and $-\pi/4$ directions, respectively. This explains why the GTF transform can detect multiorientation and high-order variations of the images.

6.3. Quantification of reconstructions

We define the image quality metrics used in this study, as follows:

(i) **Contrast-to-noise ratio (CNR)**: A local quality metric, CNR, of images is used to measure the conspicuity of the lesions. Too low CNR might result in inability of an observer to detect a lesion. The CNR for a reconstructed image is defined as a ratio of a lesion contrast to the background noise

$$CNR := |m_i - m_{bkg}|/s_{bkg}.$$

Here, for the Gaussian hot spheres in the lumpy background phantom, the m_i is the mean of reconstructed counts for the ith sphere, and the mean counts of the background, m_{bkg}, is estimated in a circular region-of-interest(ROI)located within the central region that does not intersect any sphere. The standard deviation of the background is denoted by s_{bkg}.

(ii) **Ensemble variance image (EVI)**: Ensemble variance is a metric that can be used to measure the overall image quality, as well as the sensitivity of algorithmic parameters with respect to multiple noise realizations. It is defined as [51]

$$Var := \frac{1}{N-1}\sum_{j=1}^{N}(f_j - \bar{f})^2,$$

where N is the number of noise realizations, while f_j is the reconstructed activity at noise realization j, and $\bar{f} = 1/N\sum_{j=1}^{N} f_j$ is the average activity over N noise realizations.

(iii) **Background ensemble noise (BEN)**: BEN provides a useful metric of noise across independent realizations, because it is inversely proportional to detection-task performance. For the $k-th$ region-of-interest ROI_k ($k = 1, 2, \ldots, K$ and K is the total number of background ROI), the BEN is defined as the variance of ROI mean activity $m_{j,k}$ across multiple noise realizations $j = 1, 2, \ldots, N$ [51]

$$\sigma^2_{\text{ensemble},k} := \frac{1}{N-1}\sum_{j=1}^{N}(m_{j,k} - \bar{m}_k)^2,$$

where $\bar{m}_k = 1/N\sum_{j=1}^{N} m_{j,k}$ is the average of mean activities in ROI_k over N noise realizations, and $\sigma^2_{\text{ensemble},k}$ is defined for each ROI_k. We can further average this variance over the K background $ROIs$ to generate the final BEN metric $\sigma^2_{\text{ensemble}} = \frac{1}{K}\sum_{k=1}^{K}\sigma^2_{\text{ensemble},k}$.

(iv) **Normalized mean squared error (NMSE)**: The NMSE can be used to assess accuracy of reconstructions. It is a global image quality metric and quantifies the difference between the activity reconstruction f^k and the true mean activity $f_\star$ in the whole object. It is defined by

$$NMSE := \|f^k - f_\star\|_2^2/\|f_\star\|_2^2.$$

(v) **Channelized hotelling observer (CHO)**: CHO is another important metric for investigating lesion detectability. It is widely accepted that the CHO correlates well with human observer when using proper channels and an optimal internal noise model. We select five channels, as follows: 1/64-1/32, 1/32-1/16, 1/16-1/8, 1/8-1/4, 1/4-1/2 cycles/pixel. To quantify the CHO signal-to-noise ratios (SNRs) for Gaussian sphere phantom reconstructions, we calculate the full width at half maximum (FWHM) for each Gaussian hot sphere. The corresponding values are 21.2, 18.8, 16.5, 14.1, 11.7, and 9.4 mm. For each method, 300 noise realizations are investigated.

6.4. Parameter selection

Using a task-based strategy, we independently optimize penalty parameters for each metric. In the case of CNR, we use the smallest sphere in the Gaussian hot sphere phantom. The optimal value of the TV-type hyperparameter(s) λ for TV-PAPA (λ_1, λ_2 for HOTV-PAPA) are obtained by performing sets of trial reconstructions with λ ranging from 0.5 to 10 (λ_1 ranging from 0.5 to 10, and λ_2 ranging from 0.5 to 10). For the L0METF-PFPA method, as shown in algorithm 1, we have three parameters to optimize, namely, λ, β, and initial τ. We use λ ranging from 0.008 to 0.035, β ranging from 4×10^{-7} to 1×10^{-5}, and τ ranging from 2×10^4 to 9.5×10^5. For GPF-EM, we choose the standard deviation (radius) of the Gaussian post-filter σ ranging from 1 to 4. We note that tuning parameters is a time consuming and tedious effort, especially for our method, which has three parameters. Table 1 displays the task-optimized parameters for each metric and for both noise levels. We note that both of parameters, λ and β, act as penalty weights in our proposed method.

The algorithmic parameters introduced by TV-PAPA, HOTV-PAPA are estimated by the equalities described in [30]. The algorithmic parameter τ in algorithm 1 is tuned by using an adaptive strategy. For comparison, 100 iterations are used for all the algorithms. In fact, for predefined tolerance value *tol*, one can terminate the iterative process of an algorithm when the following requirement is satisfied

$$\|f^k - f^{(k-1)}\| / \|f^k\| \leqslant tol.$$

In the numerical experiments, we establish that under the stopping criterion of 100 iterations, the relative errors $\|f^k - f^{k-1}\| / \|f^k\|$ of the three competing methods TV-PAPA, HOTV-PAPA, and L0METF-PFPA are always lower than 10^{-3}.

6.5. Results

We access the performance of the competing methods by measuring CNR, visually assessing the images with optimized CNR, analyzing background noise properties using BEN measurement and EVI, quantifying the overall reconstruction error via the NMSE, and examining hot lesions detectability using CHO. We also discuss some aspects of the subjective characteristics of the reconstructed images.

(i) *CNR Comparison*: For CNR comparisons, the spheres regions-of-interest (ROIs) are selected within the six spheres and the background region in the central disk that do not intersect with any sphere. The CNR values corresponding to the ROIs from the biggest sphere to the smallest, in counterclockwise direction, as shown in figure 1, are denoted by S1, S2, S3, S4, S5, and S6, respectively. Tables 2 and 3 show the CNR values of images reconstructed by GPF-EM, TV-PAPA, HOTV-PAPA, and L0METF-PFPA method for different noise level data, respectively. As expected, CNRs of GPF-EM are the lowest among the four methods. The L0METF-PFPA method outperforms other three methods significantly in terms of CNR, especially for low-count (64k) projection data.

(ii) *CNR-optimized Reconstructed Images*: Figure 4 displays reconstructed examples of GPF-EM, TV-PAPA, HOTV-PAPA and L0METF-PFPA for different noise levels, corresponding to the images with best CNR. After reviewing the reconstructed images, several observations can be made. First, TV-PAPA, HOTV-PAPA, and L0METF-PFPA have a better noise-suppression ability than GPF-EM. Second, for images reconstructed using TV-PAPA, HOTV-PAPA the staircase artifacts are more apparent with lower count projection data (64 K counts). Third, L0METF-PFPA suppresses staircase artifacts, even for

Table 2. Comparison of CNRs obtained for SPECT data with 90 K counts per projection for GPF-EM with $\sigma = 2.6$, TV-PAPA with $\lambda = 6$, HOTV-PAPA with $(\lambda_1, \lambda_2) = (5, 1)$, and L0METF-PFPA with $(\lambda, \beta, \tau) = (1.9 \times 10^{-2}, 4 \times 10^{-6}, 1.7 \times 10^{5})$.

Method	S1	S2	S3	S4	S5	S6
GPF-EM	23.8	21.2	19.3	13.3	12.9	7.0
TV-PAPA	34.1	31.2	27.2	23.3	22.2	11.5
HOTV-PAPA	35.9	32.4	28.9	23.9	22.8	11.9
L0METF-PFPA	**46.5**	**42.0**	**37.6**	**30.6**	**30.1**	**13.0**

Table 3. Comparison of CNRs obtained for SPECT data with 64 K counts per projection for GPF-EM with $\sigma = 2.8$, TV-PAPA with $\lambda = 6.5$, HOTV-PAPA with $(\lambda_1, \lambda_2) = (4, 1.5)$, and L0METF-PFPA with $(\lambda, \beta, \tau) = (1.3 \times 10^{-2}, 2 \times 10^{-6}, 3.5 \times 10^{5})$.

Method	S1	S2	S3	S4	S5	S6
GPF-EM	18.1	15.1	14.7	10.1	8.9	5.0
TV-PAPA	26.3	21.2	21.8	15.5	14.4	10.2
HOTV-PAPA	27.4	22.9	22.8	16.9	14.8	10.7
L0METF-PFPA	**38.9**	**32.3**	**32.5**	**23.3**	**21.5**	**13.5**

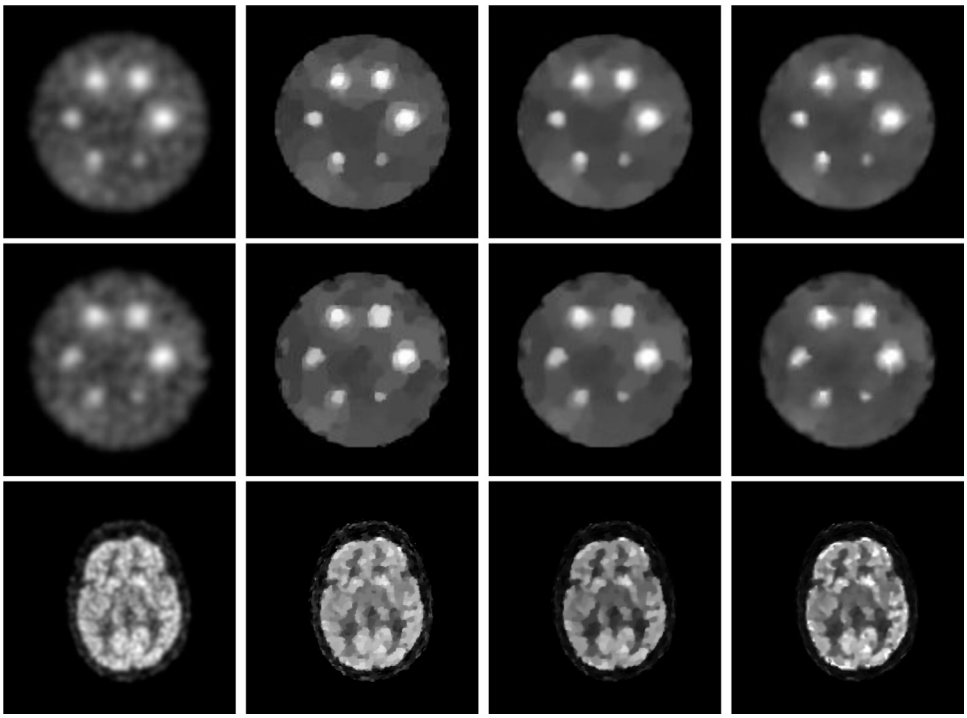

Figure 4. Images from the first column to the fourth column were respectively reconstructed by GPF-EM, TV-PAPA, HOTV-PAPA, and L0METF-PFPA at the 100th iteration. The first row and the second row correspond to 90 K and 64 K counts, respectively. Reconstructions in the third row correspond to the anthropomorphic brain phantom with 390 K counts.

Table 4. Comparison of BEN values for reconstructions by GPF-EM, TV-PAPA, HOTV-PAPA, and L0METF-PFPA.

Method	Low-noise phantom	High-noise phantom
GPF-EM	3.51×10^{-5}	2.40×10^{-5}
TV-PAPA	3.27×10^{-5}	1.61×10^{-5}
HOTV-PAPA	2.07×10^{-5}	1.62×10^{-5}
L0METF-PFPA	$\mathbf{1.03}\times10^{-5}$	$\mathbf{1.21}\times10^{-5}$

data with 64 K counts per projection. Finally, HOTV-PAPA and L0METF-PFPA perceptual image quality is better than GPF-EM and TV-PAPA, and our proposed method better suppresses staircase artifacts than HOTV-PAPA. Images in the third row in figure 4 are reconstructed for the anthropomorphic brain phantom by the four methods. In figure 6, horizontal line profiles are provided to access the differences between images reconstructed by TV-PAPA, HOTV-PAPA, and L0METF-PFPA, respectively.

(iii) *BEN Comparison*: BEN is calculated using 300 noise realizations of 7 background ROIs, which do not intersect with any sphere. Following the task-based parameter tuning strategy, parameter choices are different from that used for CNR. The results are shown in table 4, where we observe that L0METF-PFPA surpasses the other methods. We note that despite the fact that perceptually the images reconstructed by HOTV-PAPA and L0METF-PFPA appear very similar for data with 64 K counts per projection, there is substantial noise reduction in L0METF-PFPA compared to HOTV-PAPA. This shows that using appropriate tight framelet systems, combined with Moreau envelope of ℓ_0 norm, results in better noise suppression effect, as compared to the total variation transform models.

(iv) *Mean Images and Ensemble Variance Images*: We access the mean images and EVIs using the same multiple noise realizations that are used for analyzing the ensemble noise. In figure 5, different features of variance images can be appreciated. Edge artifacts have stronger variance for images reconstructed by TV-PAPA than that of HOTV-PAPA, and L0METF-PFPA. That is, the TV-PAPA variance images have the strongest edge artifacts while GPF-EM the slightest. The GPF-EM exhibits almost no edge artifacts. When considering the mean images for the high-noise data, we find that the smallest spheres are relatively difficult to discern. This is reasonable because images obtained from high-noise data exhibit reduction in contrast.

(v) *NMSE Comparison*: We calculate the NMSE for SPECT data simulated for Gaussian spheres phantom reconstructed at two noise levels by L0METF-PFPA, HOTV-PAPA, TV-PAPA, and GPF-EM. Using NMSE-task-based parameter tuning strategy, we have performed sets of experiments for each method, assuring that the optimal parameters are estimated. Table 5 shows the results. For low-noise phantom, L0METF-PFPA is comparable with HOTV-PAPA, while both surpass the other two methods (TV and GPF). For high-noise phantom, L0METF-PFPA outperforms other three methods. We remark that our method has the best performance in terms of NMSE for the two noise levels.

(vi) *CHO Comparison*: To quantify the CHO detectability for the four methods, we calculate the full width at half maximum (FWHM) for each Gaussian hot sphere. The corresponding values are 21.2,18.8,16.5,14.1,11.7,and 9.4 mm. For each method, 300 noise realizations are conducted. Following the task-based parameter tuning strategy, the optimal CHO detectability values for each method are estimated. The results are shown in tables 6 and 7. We observe that CHO performance for L0METF-PFPA is the best, followed by HOTV-PAPA, TV-PAPA, with GPF-EM performing the worst.

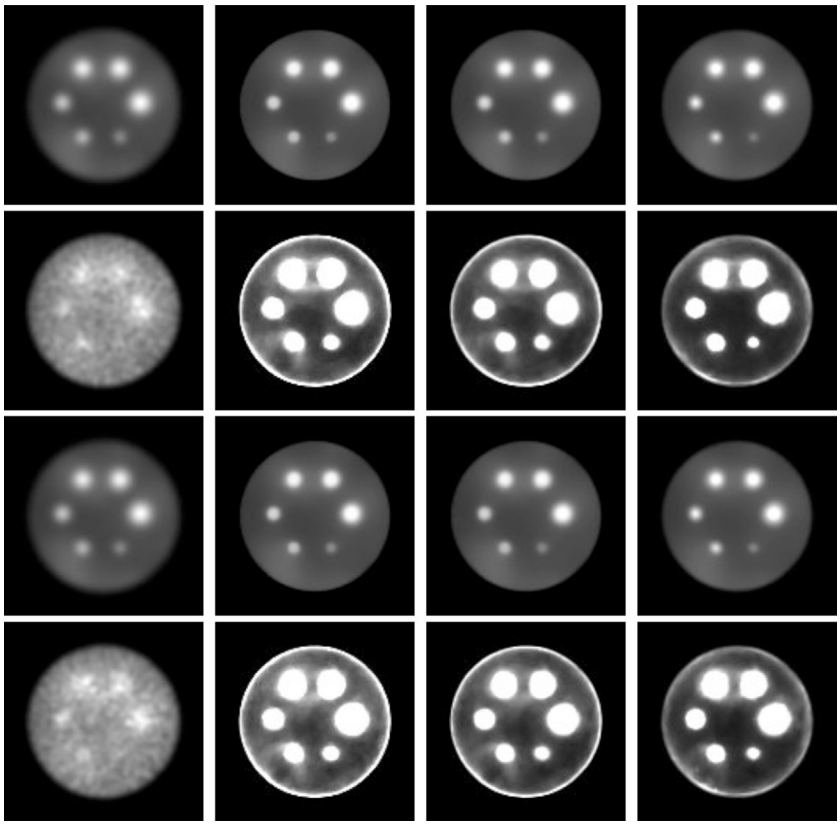

Figure 5. Mean (odd rows) and variance (even rows) images for 90 K (top two rows), and 64 K (bottom two rows) data from 300 noise realizations for GPF-EM, TV-PAPA, HOTV-PAPA, and L0METF-PFPA using 100th iterations.

Table 5. Comparison of NMSE values for reconstructions by GPF-EM, TV-PAPA, HOTV-PAPA, and L0METF-PFPA.

Method	Low-noise phantom	High-noise phantom
GPF-EM	0.042	0.048
TV-PAPA	0.026	0.039
HOTV-PAPA	**0.017**	0.027
L0METF-PFPA	**0.017**	**0.026**

(vii) *Line Profiles*: To evaluate the difference between images reconstructed by TV-PAPA, HOTV-PAPA, and L0METF-PFPA, we obtain one-channel wide line profiles through the 168th horizontal line in the reconstructed images for the anthropomorphic brain phantom. They are shown in figure 6. We observe that images reconstructed by L0METF-PFPA provide slightly better contrast and spatial resolution, as compared to those created by TV-PAPA and HOTV-PAPA, figure 4.

(viii) *Convergence Comparison*: In order to show the convergence performance of L0METF-PFPA compared to that of ML-EM, we provide plots of NMSE versus iteration number showing the convergence of L0METF-PFPA and GPF-EM for Gaussian sphere phantom reconstruction at two noise levels. We perform this comparison using

Table 6. CHOs detectability and the standard deviation of the mean values for reconstructions of projection data with 90 K counts and 300 noise realizations by GPF-EM with $\sigma = 2.7$, TV-PAPA with $\lambda = 4.5$, HOTV-PAPA with $(\lambda_1, \lambda_2) = (4, 4)$, and L0METF-PFPA with $(\lambda, \beta, \tau) = (1.8 \times 10^{-2}, 4 \times 10^{-6}, 1.72 \times 10^{5})$.

Method	21.2	18.8	16.5	14.1	11.7	9.4
GPF-EM	29.3 ± 0.9	22.7 ± 0.7	16.3 ± 0.5	16.2 ± 0.5	9.8 ± 0.3	6.2 ± 0.2
TV-PAPA	33.4 ± 1.0	32.0 ± 1.0	23.9 ± 0.7	16.5 ± 0.5	9.3 ± 0.3	5.5 ± 0.2
HOTV-PAPA	41.4 ± 1.2	36.0 ± 1.1	24.5 ± 0.7	17.1 ± 0.5	10.7 ± 0.3	5.3 ± 0.2
L0METF-PFPA	$\mathbf{55.3 \pm 1.8}$	$\mathbf{48.3 \pm 1.4}$	$\mathbf{34.3 \pm 1.0}$	$\mathbf{30.0 \pm 0.9}$	$\mathbf{16.4 \pm 0.5}$	$\mathbf{7.2 \pm 0.2}$

Table 7. CHO detectability and the standard deviation of the mean values for reconstructions of projection data with 64 K counts and 300 noise realizations by GPF-EM with $\sigma = 2.8$, TV-PAPA with $\lambda = 7$, HOTV-PAPA with $(\lambda_1, \lambda_2) = (4, 5)$, and L0METF-PFPA with $(\lambda, \beta, \tau) = (1.8 \times 10^{-2}, 1 \times 10^{-6}, 7 \times 10^{5})$.

Method	21.2	18.8	16.5	14.1	11.7	9.4
GPF-EM	24.9 ± 0.9	18.4 ± 0.6	14.7 ± 0.4	12.8 ± 0.4	7.7 ± 0.2	5.2 ± 0.2
TV-PAPA	32.9 ± 1.0	25.8 ± 0.8	19.0 ± 0.6	14.3 ± 0.4	7.7 ± 0.2	4.8 ± 0.2
HOTV-PAPA	33.1 ± 1.0	26.4 ± 0.8	18.8 ± 0.6	14.1 ± 0.4	8.3 ± 0.3	5.0 ± 0.2
L0METF-PFPA	$\mathbf{41.8 \pm 1.3}$	$\mathbf{28.0 \pm 0.8}$	$\mathbf{22.5 \pm 0.7}$	$\mathbf{15.6 \pm 0.5}$	$\mathbf{9.6 \pm 0.3}$	$\mathbf{5.5 \pm 0.2}$

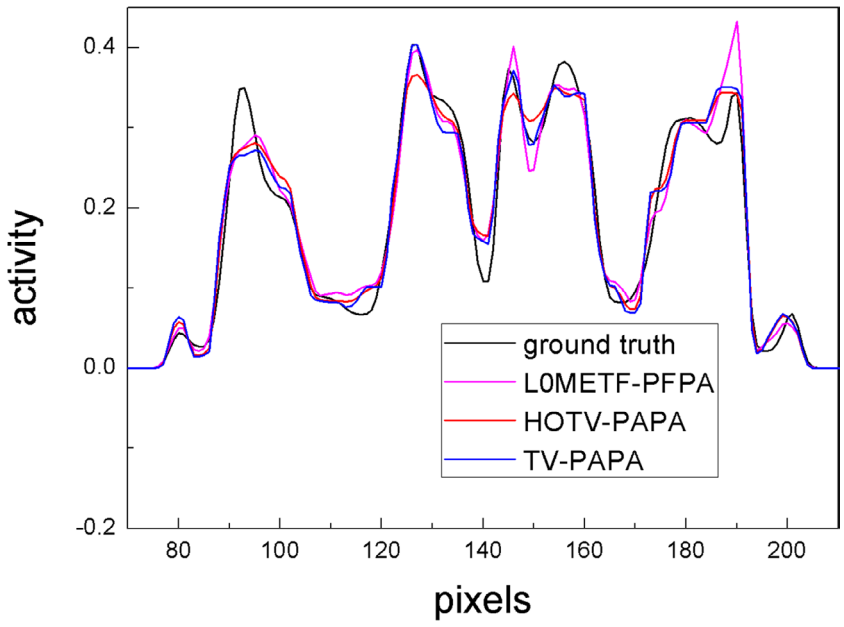

Figure 6. Horizontal line profiles through the 168th horizontal line of the reconstructed images by TV-PAPA, HOTV-PAPA, and L0METF-PFPA, compared with the ground truth.

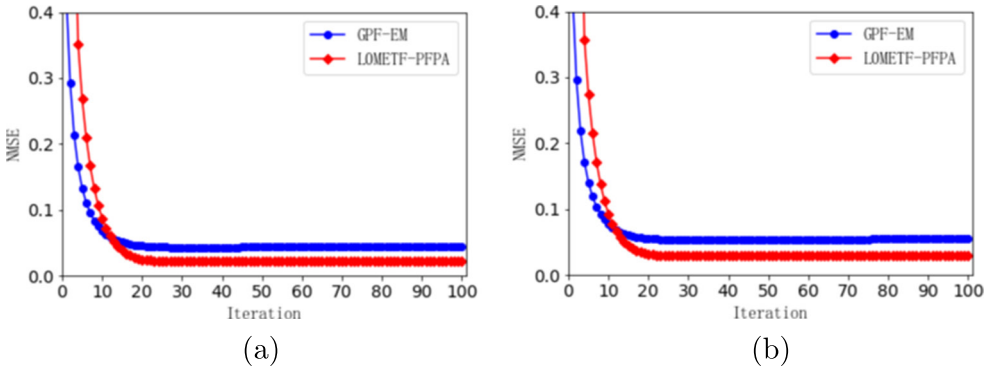

Figure 7. Plots of NMSE versus iteration number for SPECT projection data with: (a) 90 K total number of photons (low-noise phantom); and (b) 64 K total number of photons (high-noise phantom).

optimal parameters for both competing methods. In figure 7, we observe that our proposed method L0METF-PFPA has similar convergence performance to GPF-EM, while it obtains images with lower reconstruction error than GPF-EM does. We note that for now our parameter selection strategy is time-consuming, which reduces the applicability of the proposed method. Using the aggregation method proposed in [15], we will discuss the additional effort required to optimize the various parameters and develop an efficient parameter selection strategy for SPECT image reconstruction in future research.

The apparent improved resolution of the regularized images shown in figure 4 results in irregular boundaries of the 6 Gaussian spheres in the lumpy background phantom. However, the mean images demonstrate excellent registration with the reference activity distributions in the phantoms (shown in figure 5). It indicates that the improved apparent resolution is a random process stemming from the actual noise realization in the SPECT data used. Consequently, the deblurring process makes the lesion boundaries in any single realization artificially sharp and irregular. While it does not effect the performance of the tasks used in this study, it may effect segmentation tasks when conducted without taking into account the system's intrinsic resolution.

7. Conclusions

In this study, we have introduced a new model for SPECT image reconstruction which can effectively suppress noise while reconstructing by employing an approximately sparse regularization. In addition, an algorithm to efficiently solve this model has been developed. We have proved its convergence, and show that it can reach a global $\mathcal{O}(1/k)$ convergence rate. We call this method L0METF-PFPA, and compare it to the widely used EM algorithm with Gaussian post-filter smoothing (GPF-EM), and two recently developed TV-type methods: TV-PAPA and HOTV-PAPA, where, TV-PAPA corresponds to a model with first-order total variation penalty function, and HOTV-PAPA to a model with both first- and second-order total variation. To investigate the performance of L0METF-PFPA, a 2D phantom with lumpy background has been generated for two different noise levels in SPECT projection data sets. We analyze the reconstructed images quantitatively and qualitatively via the contrast-to-noise ratio (CNR), background ensemble noise (BEN), normalized mean squared error (NMSE),

and channelized hotelling observer (CHO) detectability. We also use a simulated anthropomorphic brain phantom SPECT data and compare the performance of L0METF-PFPA with TV-PAPA and HOTV-PAPA by analyzing line profiles.

In all but one case (low-noise NMSE, where it tied HOTV), we have shown that our L0METF-PFPA method outperforms the GPF-EM approach, and both the TV-type methods (TV-PAPA and HOTV-PAPA), in terms of CNR, BEN, NMSE, and CHO detectability. When investigating the difference between the reconstructions and the reference images (using NMSE as metric), we find that L0METF-PFPA is comparable with HOTV-PAPA for low-noise data and outperforms all the evaluated methods for high-noise data. These results are consistent with our subjective image quality assessments. Further, we establish that images reconstructed by L0METF-PFPA demonstrate higher contrast. We conclude that our proposed method based on Moreau envelope of ℓ_0 norm as a penalty function in the tight framelet transform domain for SPECT reconstruction provides an effective means of noise suppression, and hence can lead to improved quality in SPECT reconstruction. Consequently, it may allow use of higher noise data i.e. the lower radiation dose or shorter imaging time in SPECT studies, as compared to conventional GPF-EM approach.

Acknowledgments

This research was partially supported by the Special Project on High-performance Computing under the National Key R&D Program (No. 2016YFB0200602), and by National Natural Science Foundation of China under Grants 11471013, 11571383, 11601537, 11771464 and 11701538, by the National Institutes of Health/National Cancer Institute Cancer Center support Grant P30 CA008748, by the Science and Technology Program of Guangzhou, China under Grant 201804020053. Y Xu was also partially supported by US National Science Foundation under grant DMS-1912958.

ORCID iDs

C Ross Schmidtlein https://orcid.org/0000-0003-0485-3601
Yuesheng Xu https://orcid.org/0000-0003-2982-7864

References

[1] Abbey C K, Barrett H H and Wilson D W 1996 Observer signal-to-noise ratios for the ml-em algorithm *Proc. SPIE* **2712** 47–58
[2] Attouch H, Bolte J, Redont P and Soubeyran A 2010 Proximal alternating minimization and projection methods for nonconvex problems: an approach based on the Kurdyka–Łojasiewicz inequality *Math. Oper. Res.* **35** 438–57
[3] Attouch H, Bolte J and Svaiter B F 2013 Convergence of descent methods for semi-algebraic and tame problems: proximal algorithms, forward–backward splitting, and regularized Gauss–Seidel methods *Math. Program.* **137** 91–129
[4] Bao C, Dong B, Hou L, Shen Z, Zhang X and Zhang X 2016 Image restoration by minimizing zero norm of wavelet frame coefficients *Inverse Problems* **32** 115004
[5] Bauschke H H and Combettes P L 2011 *Convex Analysis and Monotone Operator Theory in Hilbert Spaces* (New York: Springer)
[6] Beck A and Teboulle M 2009 A fast iterative shrinkage-thresholding algorithm for linear inverse problems *SIAM J. Imaging Sci.* **2** 183–202

[7] Bertero M, Boccacci P, Desidera G and Vicidomini G 2009 Image deblurring with poisson data: from cells to galaxies *Inverse Problems* **25** 123006
[8] Blumensath T and Davies M E 2009 Iterative hard thresholding for compressed sensing *Appl. Comput. Harmon. Anal.* **27** 265–74
[9] Bolte J, Sabach S and Teboulle M 2014 Proximal alternating linearized minimization for nonconvex and nonsmooth problems *Math. Program.* **146** 459–94
[10] Boyd S and Vandenberghe L 2004 *Convex Optimization* (Cambridge: Cambridge University Press)
[11] Bruckstein A M, Donoho D L and Elad M 2009 From sparse solutions of systems of equations to sparse modeling of signals and images *SIAM Rev.* **51** 34–81
[12] Candes E J, Romberg J K and Tao T 2006 Robust uncertainty principles: exact signal reconstruction from highly incomplete frequency information *IEEE Trans. Inf. Theory* **52** 489–509
[13] Chan R H, Chan T F, Shen L and Shen Z 2003 Wavelet algorithms for high-resolution image reconstruction *SIAM J. Sci. Comput.* **24** 1408–32
[14] Chan R H, Riemenschneider S D, Shen L and Shen Z 2004 Tight frame: an efficient way for high-resolution image reconstruction *Appl. Comput. Harmon. Anal.* **17** 91–115
[15] Chen J, Pereverzyev S and Xu Y 2015 Aggregation of regularized solutions from multiple observation models *Inverse Problems* **31** 075005
[16] Chen S, Liu H, Shi P and Chen Y 2015 Sparse representation and dictionary learning penalized image reconstruction for positron emission tomography *Phys. Med. Biol.* **60** 807–23
[17] Csisz I 1991 Why least squares and maximum entropy? An axiomatic approach to inference for linear inverse problems *Ann. Stat.* **19** 2032–66
[18] Daubechies I 1992 *Ten Lectures on Wavelets* (Philadelphia, PA: SIAM)
[19] Dewaraja Y K, Koral K F and Fessler J A 2010 Regularized reconstruction in quantitative SPECT using CT side information from hybrid imaging *Phys. Med. Biol.* **55** 2523–39
[20] Ding Q, Zan Y, Huang Q and Zhang X 2015 Dynamic SPECT reconstruction from few projections: a sparsity enforced matrix factorization approach *Inverse Problems* **31** 025004
[21] Donoho D L 2006 Compressed sensing *IEEE Trans. Inf. Theory* **52** 1289–306
[22] Elad M 2010 *Sparse and Redundant Representations: from Theory to Applications in Signal and Image Processing* (New York: Springer)
[23] Fessler J A and Rogers W L 1996 Spatial resolution properties of penalized-likelihood image reconstruction: space-invariant tomographs *IEEE Trans. Image Process.* **5** 1346–58
[24] Geman S and Geman D 1984 Stochastic relaxation, gibbs distributions, and the bayesian restoration of images *IEEE Trans. Pattern Anal. Mach. Intell.* **6** 721–41
[25] Green P 1990 Bayesian reconstructions from emission tomography data using a modified em algorithm *IEEE Trans. Med. Imaging* **9** 84–93
[26] Hudson H M and Larkin R S 1994 Accelerated image reconstruction using ordered subsets of projection data *IEEE Trans. Med. Imaging* **13** 601–9
[27] Joshi S H, Marquina A, Osher S J, Dinov I, Van Horn J D and Toga A W 2009 MRI resolution enhancement using total variation regularization *IEEE Int. Symp. on Biomedical Imaging* pp 161–4
[28] Krol A, Li S, Shen L and Xu Y 2012 Preconditioned alternating projection algorithms for maximum *a posteriori* ECT reconstruction *Inverse Problems* **28** 115005
[29] Lange K *et al* 1984 EM reconstruction algorithms for emission and transmission tomography *J. Comput. Assist. Tomogr.* **8** 306–16
[30] Li S, Zhang J, Krol A, Schmidtlein C R, Vogelsang L, Shen L, Lipson E, Feiglin D and Xu Y 2015 Effective noise-suppressed and artifact-reduced reconstruction of SPECT data using a preconditioned alternating projection algorithm *Med. Phys.* **42** 4872–87
[31] Li Y-R, Dai D-Q and Shen L 2010 Multiframe super-resolution reconstruction using sparse directional regularization *IEEE Trans. Circuits Syst. Video Technol.* **20** 945–56
[32] Lian Q, Shen L, Xu Y and Yang L 2011 Filters of wavelets on invariant sets for image denoising *Appl. Anal.* **90** 1299–322
[33] Micchelli C A, Shen L and Xu Y 2011 Proximity algorithms for image models: denoising *Inverse Problems* **27** 045009
[34] Micchelli C A, Shen L, Xu Y and Zeng X 2013 Proximity algorithms for the L1/TV image denoising model *Adv. Comput. Math.* **38** 401–26
[35] Moreau J-J 1962 Fonctions convexes duales et points proximaux dans un espace hilbertien *C. R. Acad. Sci. Paris* **255** 2897–9
[36] Natarajan B K 1995 Sparse approximate solutions to linear systems *SIAM J. Comput.* **24** 227–34

[37] Natterer F and Wübbeling F 2001 *Mathematical Methods in Image Reconstruction* vol 5 (Philadelphia, PA: SIAM)
[38] Panin V Y, Zeng G L and Gullberg G T 1999 Total variation regulated EM algorithm [SPECT reconstruction] *IEEE Trans. Nucl. Sci.* **46** 2202–10
[39] Persson M, Bone D and Elmqvist H 2001 Total variation norm for three-dimensional iterative reconstruction in limited view angle tomography *Phys. Med. Biol.* **46** 853–66
[40] Ritschl L, Bergner F, Fleischmann C and Kachelries M 2011 Improved total variation-based CT image reconstruction applied to clinical data *Phys. Med. Biol.* **56** 1545–61
[41] Rockafellar R T and Wets R J-B 2009 *Variational Analysis* vol 317 (Berlin: Springer)
[42] Rolland J P and Barrett H H 1992 Effect of random background inhomogeneity on observer detection performance *J. Opt. Soc. Am.* A **9** 649–58
[43] Ron A and Shen Z 1997 Affine systems in $l_2(\mathbf{R}^d)$: the analysis of the analysis operator *J. Funct. Anal.* **148** 408–47
[44] Rudin L I, Osher S and Fatemi E 1992 Nonlinear total variation based noise removal algorithms *Physica* D **60** 259–68
[45] Sawatzky A, Brune C, Wubbeling F, Kosters T, Schafers K and Burger M 2008 Accurate EM-TV algorithm in PET with low SNR *IEEE Nuclear Science Symp. Conf. Record* (IEEE) pp 5133–7
[46] Shen L, Papadakis M, Kakadiaris I A, Konstantinidis I, Kouri D J and Hoffman D K 2006 Image denoising using a tight frame *IEEE Trans. Image Process.* **15** 1254–63
[47] Shen L, Xu Y and Zeng X 2016 Wavelet inpainting with the ℓ_0 sparse regularization *Appl. Comput. Harmon. Anal.* **41** 26–53
[48] Shepp L, Vardi Y, Ra J B, Hilal S K and Cho Z H 1984 Maximum likelihood PET with real data *IEEE Trans. Nucl. Sci.* **31** 910–3
[49] Shepp L A and Vardi Y 1982 Maximum likelihood reconstruction for emission tomography *IEEE Trans. Med. Imaging* **1** 113–22
[50] Sidky E Y and Pan X 2008 Image reconstruction in circular cone-beam computed tomography by constrained, total-variation minimization *Phys. Med. Biol.* **53** 4777–807
[51] Tong S, Alessio A M and Kinahan P E 2010 Noise and signal properties in PSF-based fully 3D PET image reconstruction: an experimental evaluation *Phys. Med. Biol.* **55** 1453–73
[52] Tropp J A 2006 Just relax: convex programming methods for identifying sparse signals in noise *IEEE Trans. Inf. Theory* **52** 1030–51
[53] Tropp J A, Gilbert A C and Strauss M J 2006 Algorithms for simultaneous sparse approximation: part I: greedy pursuit *Signal Process.* **86** 572–88
[54] Wernick M N and Aarsvold J N 2004 *Emission Tomography: the Fundamentals of PET and SPECT* (New York: Academic)
[55] Wu Z, Li S, Zeng X, Xu Y and Krol A 2016 Reducing staircasing artifacts in SPECT reconstruction by an infimal convolution regularization *J. Comput. Math.* **34** 626–47
[56] Xu Q, Yu H, Mou X, Zhang L, Hsieh J and Wang G 2012 Low-dose x-ray CT reconstruction via dictionary learning *IEEE Trans. Med. Imaging* **31** 1682–97
[57] Zanella R, Boccacci P, Zanni L and Bertero M 2013 Efficient gradient projection methods for edge-preserving removal of poisson noise *Inverse Problems* **25** 045010
[58] Zeng X, Shen L and Xu Y 2018 A convergent fixed-point proximity algorithm accelerated by FISTA for the ℓ_0 sparse recovery problem *Imaging, Vision and Learning Based on Optimization and PDEs* ed X-C Tai *et al* (Cham: Springer) pp 27–45
[59] Zhang J, Li S, Xu Y, Schmidtlein C R, Lipson E D, Feiglin D H and Krol A 2015 SPECT reconstruction using DCT-induced tight framelet regularization *Proc. SPIE* **9412** 94123H
[60] Zhang Y, Dong B and Lu Z 2013 ℓ_0 minimization for wavelet frame based image restoration *Math. Comput.* **82** 995–1015
[61] Zhou W, Cai J-F and Gao H 2013 Adaptive tight frame based medical image reconstruction: a proof-of-concept study for computed tomography *Inverse problems* **29** 125006